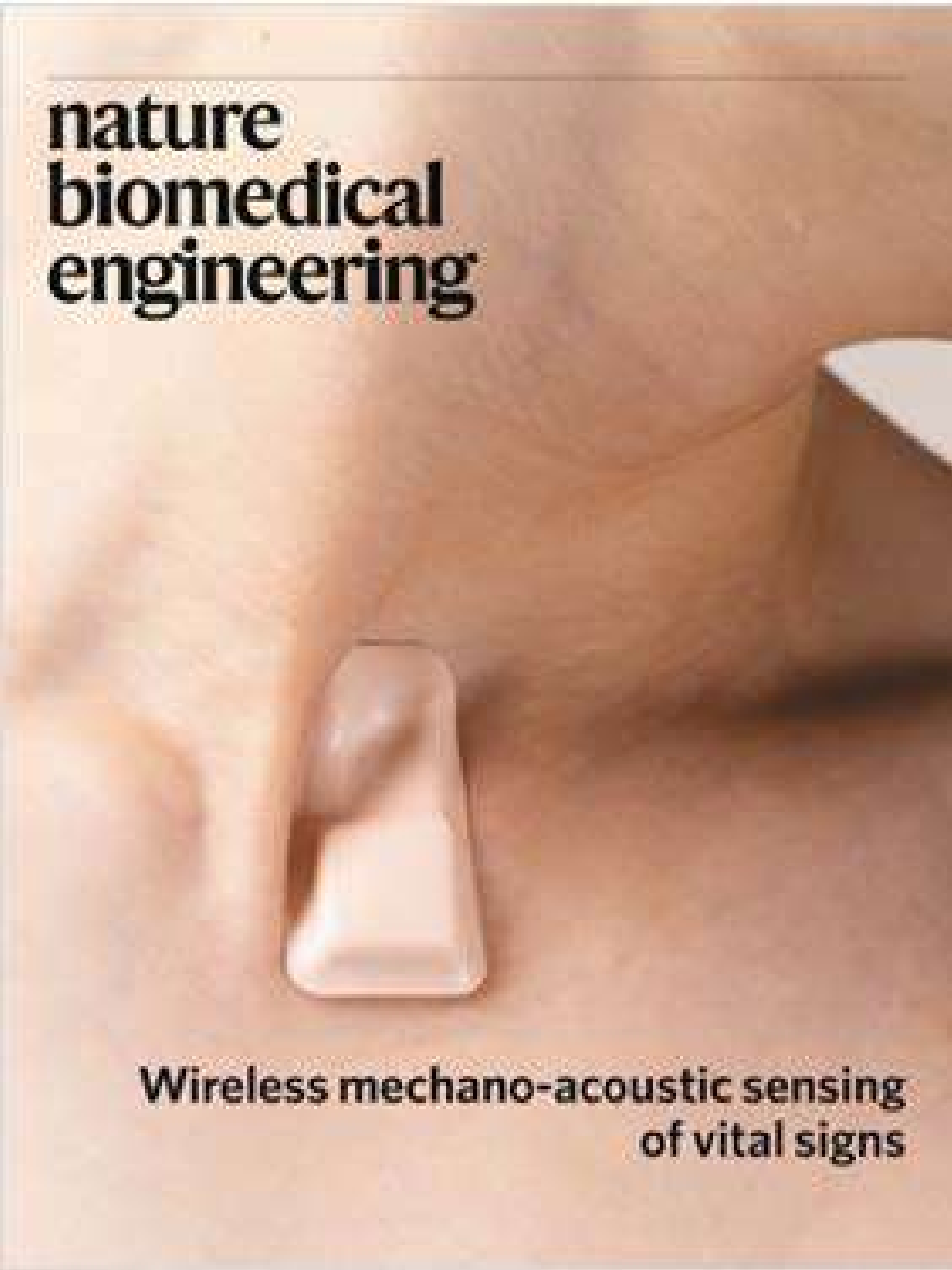


nature biomedical engineering



**Wireless mechano-acoustic sensing
of vital signs**

Mechano-acoustic sensing of physiological processes and body motions via a soft wireless device placed at the suprasternal notch

KunHyuck Lee^{1,2,21}, Xiaoyue Ni^{3,21}, Jong Yoon Lee^{3,21}, Hany Arafa^{1,4}, David J. Pe⁵, Shuai Xu^{1,3,6}, Raudel Avila^{2,3,7,8}, Masahiro Irie^{1,9}, Joo Hee Lee³, Ryder L. Easterlin¹⁰, Dong Hyun Kim¹¹, Ha Uk Chung^{1,9}, Omolara O. Olabisi⁴, Selam Getaneh⁸, Esther Chung⁴, Marc Hill⁴, Jeremy Bell¹², Hokyung Jang³, Claire Liu^{1,4}, Jun Bin Park¹³, Jungwoo Kim³, Sung Bong Kim¹⁴, Sunita Mehta³, Matt Pharr¹⁵, Andreas Tzavelis¹⁶, Jonathan T. Reeder^{2,3}, Ivy Huang^{1,2}, Yujun Deng^{2,3,7,8,17}, Zhaoqian Xie^{1,2,3,7,8,18*}, Charles R. Davies^{19*}, Yonggang Huang^{2,3,7,8*} and John A. Rogers^{1,2,3,4,5,8,9,20*}

Skin-mounted soft electronics that incorporate high-bandwidth triaxial accelerometers can capture broad classes of physiologically relevant information, including mechano-acoustic signatures of underlying body processes (such as those measured by a stethoscope) and precision kinematics of core-body motions. Here, we describe a wireless device designed to be conformally placed on the suprasternal notch for the continuous measurement of mechano-acoustic signals, from subtle vibrations of the skin at accelerations of around 10^{-3} m s^{-2} to large motions of the entire body at about 10 m s^{-2} , and at frequencies up to around 800 Hz. Because the measurements are a complex superposition of signals that arise from locomotion, body orientation, swallowing, respiration, cardiac activity, vocal-fold vibrations and other sources, we exploited frequency-domain analysis and machine learning to obtain—from human subjects during natural daily activities and exercise—real-time recordings of heart rate, respiration rate, energy intensity and other essential vital signs, as well as talking time and cadence, swallow counts and patterns, and other unconventional biomarkers. We also used the device in sleep laboratories and validated the measurements using polysomnography.

Natural processes of the human body yield a multitude of mechano-acoustic (MA) signals, many of which strongly attenuate at the skin–air interface^{1–5}. Motions with amplitudes and frequencies ranging from subtle vibrations to full-body kinematics contain diverse and important physiological health information. Examples include vocal-fold vibrations (about 100 Hz), cardiac activity (about 10 Hz), gait and locomotion (about 1 Hz), respiration (about 0.1 Hz) and body orientation (about 0 Hz). Digital stethoscopes and inertial measurement units represent clinical-grade tools that quantitatively capture some of these and other MA data^{6–9}. Digital stethoscopes acquire signals typically confined to a frequency range of 20 to 1,900 Hz, non-continuously and episodically⁸.

Traditional inertial measurement units can be used continuously, but they are most effective at low frequencies (0–100 Hz) due mainly to their high inertial mass and loose coupling to the body^{9,10}. These types of sensors cannot capture both mechanical and acoustic aspects of MA signals simultaneously with high fidelity. Compact, skin-mounted accelerometers and/or gyroscopes based on micro-electromechanical systems offer important capabilities in this context, with demonstrated examples of capturing signatures of cardiac mechanics, such as seismocardiograms or ballistocardiograms^{11–14}, respiratory rate and sounds^{15–21}, sounds of swallowing^{22–25}, vocals^{26,27}, changes in body position and motion^{28–30} and others³¹. Some of these measurements have direct relevance to medical applications,

¹Simpson Querry Institute, Northwestern University, Chicago, IL, USA. ²Department of Materials Science and Engineering, Northwestern University, Evanston, IL, USA. ³Center for Bio-Integrated Electronics, Northwestern University, Evanston, IL, USA. ⁴Department of Biomedical Engineering, Northwestern University, Evanston, IL, USA. ⁵Department of Chemistry, Northwestern University, Evanston, IL, USA. ⁶Department of Dermatology, Feinberg School of Medicine, Northwestern University, Chicago, IL, USA. ⁷Department of Civil and Environmental Engineering, Northwestern University, Evanston, IL, USA. ⁸Department of Mechanical Engineering, Northwestern University, Evanston, IL, USA. ⁹Department of Electrical and Computer Engineering, Northwestern University, Evanston, IL, USA. ¹⁰Department of Molecular Biosciences, Northwestern University, Evanston, IL, USA. ¹¹Department of Electrical and Computer Engineering, University of Illinois at Urbana-Champaign, Urbana, IL, USA. ¹²Department of Economics, Northwestern University, Evanston, IL, USA. ¹³Department of Statistics, University of Illinois at Urbana-Champaign, Urbana, IL, USA. ¹⁴Department of Materials Science and Engineering, University of Illinois at Urbana-Champaign, Urbana, IL, USA. ¹⁵Department of Mechanical Engineering, Texas A&M University, College Station, TX, USA. ¹⁶Medical Scientist Training Program, Feinberg School of Medicine, Northwestern University, Chicago, IL, USA. ¹⁷State Key Laboratory of Mechanical System and Vibration, Shanghai Jiao Tong University, Shanghai, China. ¹⁸State Key Laboratory of Structural Analysis for Industrial Equipment, Department of Engineering Mechanics, Dalian University of Technology, Dalian, China. ¹⁹Carle Neuroscience Institute, Carle Physician Group, Urbana, IL, USA. ²⁰Department of Neurological Surgery, Northwestern University, Evanston, IL, USA. ²¹These authors contributed equally: KunHyuck Lee, Xiaoyue Ni, Jong Yoon Lee. *e-mail: xiezhaoqian@gmail.com; charles.davies@carle.com; y-huang@northwestern.edu; jrogers@northwestern.edu

particularly when implemented in devices that monitor multiple physiological signals^{1,3,32}.

Conventional wearable devices for such purposes couple to the body in the form of straps, adhesive patches or bands, with the chest or wrist serving as the measurement interface^{33–35}. Other body locations can be used, but there are substantial practical limitations that follow from the rigid, planar form factors of the devices^{26,36,37}. For example, microphones strapped to the neck can capture acoustic signals associated with speech and throat sounds for detection of dietary behaviour and respiratory physiology³⁸, and accelerometers attached to the skin of the neck with wax can record a range of body processes for tracking patterns of sleep³⁶. These types of systems cannot, however, support persistent, comfortable interfaces with the skin during normal daily activities. Soft, lightweight skin-compatible wireless devices with the ability to be mounted on unusual parts of the body can continuously track a full spectrum of mechanical and acoustic signatures of body processes. Potential applications include monitoring health status and social interactions throughout the day, quantifying sleep behaviours, measuring athletic performance and guiding rehabilitation protocols.

Recent advances in soft electronics^{1,39–43} serve as the foundation for skin-compliant, lightweight devices that incorporate accelerometers based on microelectromechanical systems technologies¹. The device in this study comprises a collection of functional components, encapsulated and supported by an elastomer and interconnected with serpentine conductive traces that maximize the measurement sensitivity by mechanically decoupling the sensing element from the supporting electronics¹. The resulting ‘epidermal’ MA sensors are highly responsive to movements and vibratory processes of the body, with the ability to capture high-quality signals across frequencies from 0 Hz to the audible band, with minimal interference from ambient noise¹.

The advances presented here build on these initial findings through (1) the design of wireless systems optimized for a comfortable skin interface and high precision, high-bandwidth MA measurements, powered with small-scale rechargeable batteries; (2) the use of the suprasternal notch (SN) as a unique anatomical mounting location that offers a rich blend of MA information related to diverse classes of physiological processes and core-body motions; (3) the development of data analysis techniques for extracting quantitative physiological insights from the resulting multimodal data; (4) the combined demonstration of the unusual mechanics of the device, unique mounting locations and advanced analytic approaches in continuous or semi-continuous monitoring during routine daily activities and physical exercise; and (5) the clinical validation of results captured in sleep laboratories through quantitative comparisons to recordings obtained by gold-standard polysomnography systems.

Results

Engineering mechanics of the device. The thin, soft form factors of the system introduced here enable skin-interfaced measurements of MA signals continuously and wirelessly at nearly any location on the body, including sensitive regions such as the SN. High data fidelity and comfortable, non-irritating interfaces are key features. Figure 1a,b outlines the overall device layout, with images that demonstrate its ability to deform naturally with movements of the neck when mounted on the SN. The design incorporates deformable, non-coplanar serpentine interconnects, a strain-isolation layer at the base, a soft-encapsulation overlayer and a hollow air-pocket configuration. Together, these features provide low-modulus, elastic mechanics despite the incorporation of conventional rigid electronic components and flexible printed circuit board technologies with layouts that are compatible with high-volume manufacturing.

Figure 1b presents, more specifically, the overall structure of the system. The device consists of a flexible printed circuit board (fPCB)

based on a 25- μm -thick middle polyimide support layer with patterned traces of 12- μm -thick rolled, annealed copper (Cu) on the top and bottom surfaces (AP7164R, DuPont), each encapsulated with an insulating layer of polyimide (25 μm , FR1510, DuPont)⁴⁴. The main electronic subsystems include (1) a three-axis digital accelerometer (BMI160, Bosch) for measuring motions with a sampling frequency and resolution of 1,600 Hz and 16 bits, respectively, a broad bandwidth response (0–1,600 Hz) and a sufficient dynamic range ($\pm 2g$) (where g is the gravitational acceleration, 9.8 m s^{-2}); (2) a microcontroller (nRF52832, Nordic Semiconductor) for acquiring data from the accelerometer and communicating the results wirelessly via Bluetooth low-energy protocols; and (3) a wireless inductive charging circuit to support a rechargeable 45 mAh lithium-ion polymer battery (Fig. 1c).

Because these subsystems rely exclusively on rigid, planar off-the-shelf components, they must be carefully integrated in a manner that simultaneously offers soft, skin-compatible mechanics as well as effective mechanical coupling of the accelerometer to the body. The schemes used here exploit advanced versions of design concepts in stretchable electronics⁴³, adapted for use with the fPCB generally, and for the interconnects between the subsystems specifically. As shown in Fig. 1b, serpentine-shaped interconnects mechanically and electrically join two rectangular regions of the fPCB (islands; $1 \text{ cm} \times 1 \text{ cm}$). One island supports the microcontroller and charging circuit. Here, the fPCB folds onto itself to minimize the area taken up by the rigid components (Fig. 1b). The other island includes the charging coil and connections to the battery. The coil includes two Cu traces (120 μm wide) in a rectangular spiral design (8 turns, 100 μm pitch) on both top and bottom sides of the fPCB. This minimizes the overall size of the device while allowing larger electromagnetic flux to go through the coil compared with a single layer coil with the same dimension. The top and bottom coils share the same polarity and dimensions (9.55 mm \times 10.7 mm). Electroplating (Contac S4) creates a conductive path across the two sides of the fPCB through holes located at the ends of the coils.

Small pieces of rigid printed circuit board material (Garolite G-10/FR4; 381 μm thick, 22 GPa modulus, McMaster Carr 1331T37) support each of the two main islands to increase their bending stiffness by three orders of magnitude (49 μm thick, 4.8 GPa modulus). This design effectively eliminates bending in these regions, thereby enhancing the robustness of the solder bonding joints between the components and the fPCB. These islands comprise 30% of the overall area of the system, leaving $\sim 70\%$ for freely deformable regions, including the serpentine-interconnect structures.

The accelerometer rests on a cantilever that extends from the component island via a thin, narrow region of the fPCB to allow effective coupling to the skin with minimal mechanical constraints from other parts of the system (dashed red outline in Fig. 1b). To prevent entanglement, the interconnects consist of two layers of serpentine wires embedded in silicone gel (Silbione 4717 Gel A/B, Elkem; 0.4 mm thick) with a low Young’s modulus (6 kPa) to minimize constraints on deformation of the serpentine wires (Supplementary Fig. 1a). A pre-buckled, out-of-plane, arc-shaped geometry allows the serpentine interconnects to assume traction-free architectures that absorb tensile deformations in two distinct modes (Supplementary Figs. 1d, middle, and 2) in a manner largely decoupled from the bottom substrate of the device. Finite element analysis highlights significant mechanical advantages of these non-coplanar interconnects compared with conventional planar serpentine layouts (Supplementary Fig. 1 and Supplementary Note 2). At the optimized arc angle $\theta = 270^\circ$ and with pre-buckling, the elastic stretchability, $\epsilon = (L_y - L^*)/L^*$ (where L^* is initial length (Fig. 1d, left) and L_y is the length at which the Cu layer reaches the elastic limit) increases to 43% from 14% stretchability with arc angle $\theta = 210^\circ$ and without pre-buckling (Fig. 1d, middle and Supplementary Fig. 1b). Additional finite element analysis results

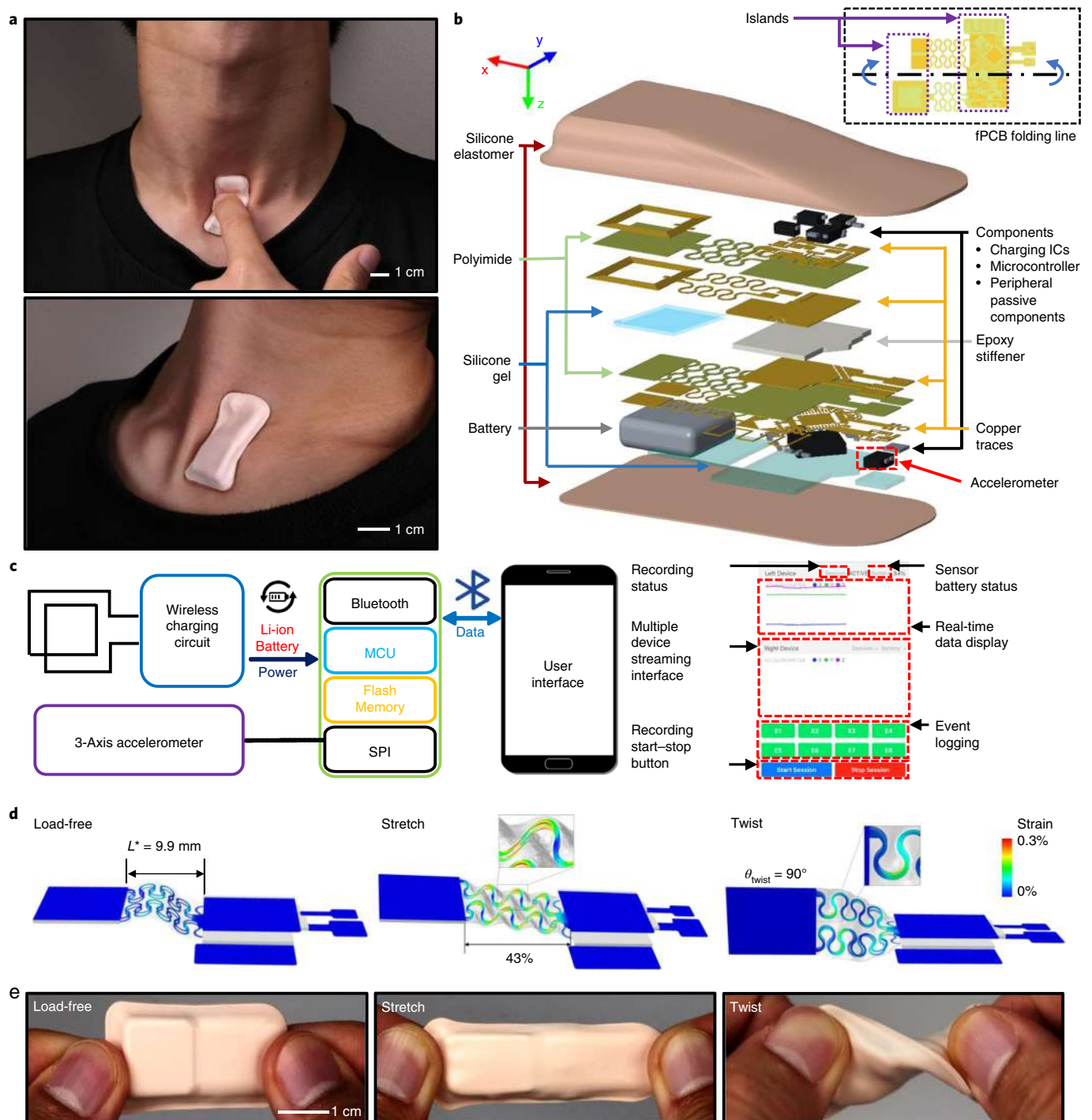


Fig. 1 | A wireless, skin-interfaced MA measurement technology designed for mounting on the SN. **a**, Images that demonstrate soft-device mechanics during movements of the neck while interfaced to the SN. **b**, Exploded schematic illustration of the active components, interconnect schemes and enclosure architectures. IC, integrated circuit. **c**, Block diagram of the system operation (Supplementary Note 1). **d**, Finite element modelling of the mechanics during uniaxial tensile and twisting deformations. **e**, Images of the device in undeformed (left), stretched (middle) and twisted (right) configurations.

indicate that the maximum effective strain in the Cu layer is significantly less than the yield strain (0.3%) under various mechanical loads (Fig. 1d, right and Supplementary Fig. 3). These results highlight the range of robust, low-modulus, elastic responses (Supplementary Figs. 4 and 5) necessary to accommodate realistic physiological motions with little constraint on the underlying skin (Fig. 1e). Supplementary Fig. 5 also shows that the fPCB thickness has little effect on the overall device modulus and stiffness. In addition

to the mechanical characterization of the complete device, Supplementary Figs. 6–8 illustrate the effect of the packaging materials and device structure on the signal fidelity. Supplementary Fig. 6 compares z-axis acceleration recordings across a frequency range of 0 to 800 Hz, measured by a complete wireless system and by a wired, isolated accelerometer. The ratio between the two measurements is close to unity across the measurement range, demonstrating that the effects of the packaging materials are negligible. As shown

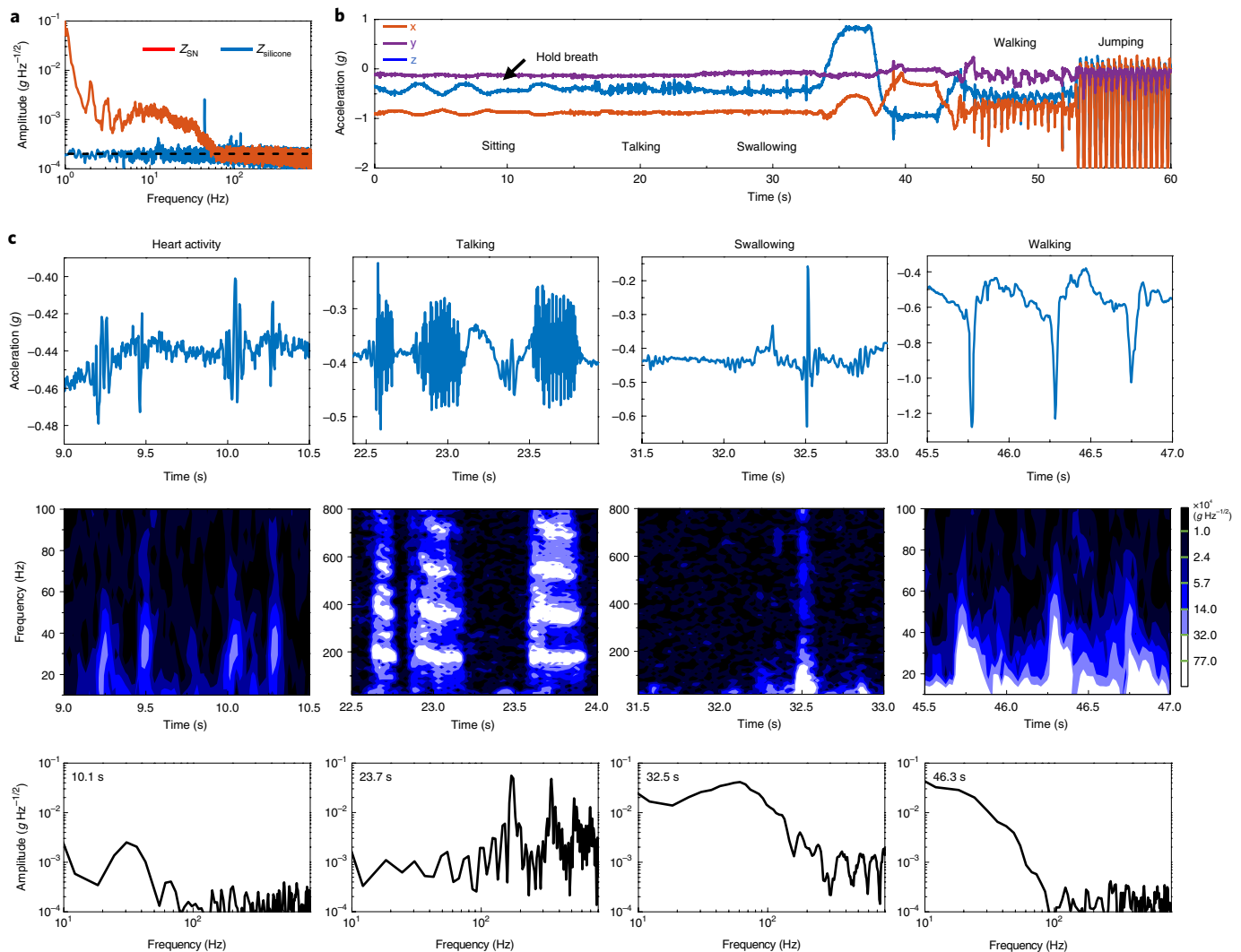


Fig. 2 | Representative MA data in the form of accelerations measured along three orthogonal axes from the MA device mounted on the SN of a healthy subject. **a**, Power spectral analysis of data (z-axis acceleration) collected from a device vertically resting on an elastomer (Z_{silicone}) and interfaced to the SN of a subject sitting quietly (Z_{sn}). The power spectrum of the measurement from the SN shows high power below 100 Hz associated with various involuntary physiological events. **b**, Three-axis time series data simultaneously recorded over a 60 s interval as a subject engages in various activities that include sitting at rest, talking, drinking water, changing body orientation, walking and jumping. **c**, Sample time-series data, spectrograms and spectral information corresponding to cardiac activity, talking, swallowing and walking. The colours indicate the amplitude spectral density. The frequency analysis uses a Hanning window with a width of 0.1 s moving in time steps of 0.02 s.

in Supplementary Figs. 7 and 8, results from a simple simulation model confirm these findings.

Data and analysis approaches for measurements from the SN.

Natural physiological processes generate diverse MA signals at the surface of the skin, from subtle vibrations on the order of $\sim 1 \times 10^{-4} \text{ g Hz}^{-1/2}$ (Fig. 2a) to large-scale motions with amplitudes of $\sim 2\text{g}$, across a band of frequencies (0 to 800 Hz) that can be captured with the accelerometers used here. The SN represents a unique anatomical location for recording such signals, as a direct soft-tissue MA interface to vital organs related to cardiovascular, respiratory and digestive systems and their interconnections between the head and torso. Figure 2a shows the typical sensitivity of the device (along the z axis, axes defined in Fig. 1b) characterized when placed on a vertical slab of elastomer (4 mm thick, 60 kPa) and when interfaced with the SN (Fig. 1a) of a subject while sitting quietly. The sensor on the slab shows nearly uniform noise power density across the entire frequency range.

At the SN, proximity to the carotid artery results in vibratory signatures related to the pulsatile flow of blood. The periodic nature of these signals allows determination of heart rate and variability. The cross-correlation of pulses measured from the chest near the pulmonary area and the SN defines a time lag between these two signals (Supplementary Fig. 9). The lag of $\sim 13 \text{ ms}$ is consistent with recordings of vibratory signatures from the carotid artery itself, as opposed to chest-body vibrations. The amplitudes yield information on the intensity of cardiac activity and, indirectly, stroke volume. Passage of air through the trachea and movements of the chest wall produce MA data related to swallowing, talking, breathing, coughing, sighing, snoring and other responses. Furthermore, the device simultaneously responds to chest-wall and full-body movements, including orientation referenced to the gravity vector.

All such signals rise well above the noise floor of the measurement system. To demonstrate the collective capabilities, Fig. 2b presents representative three-axis acceleration data recorded from the SN of a healthy subject engaged in a sequential series of activities.

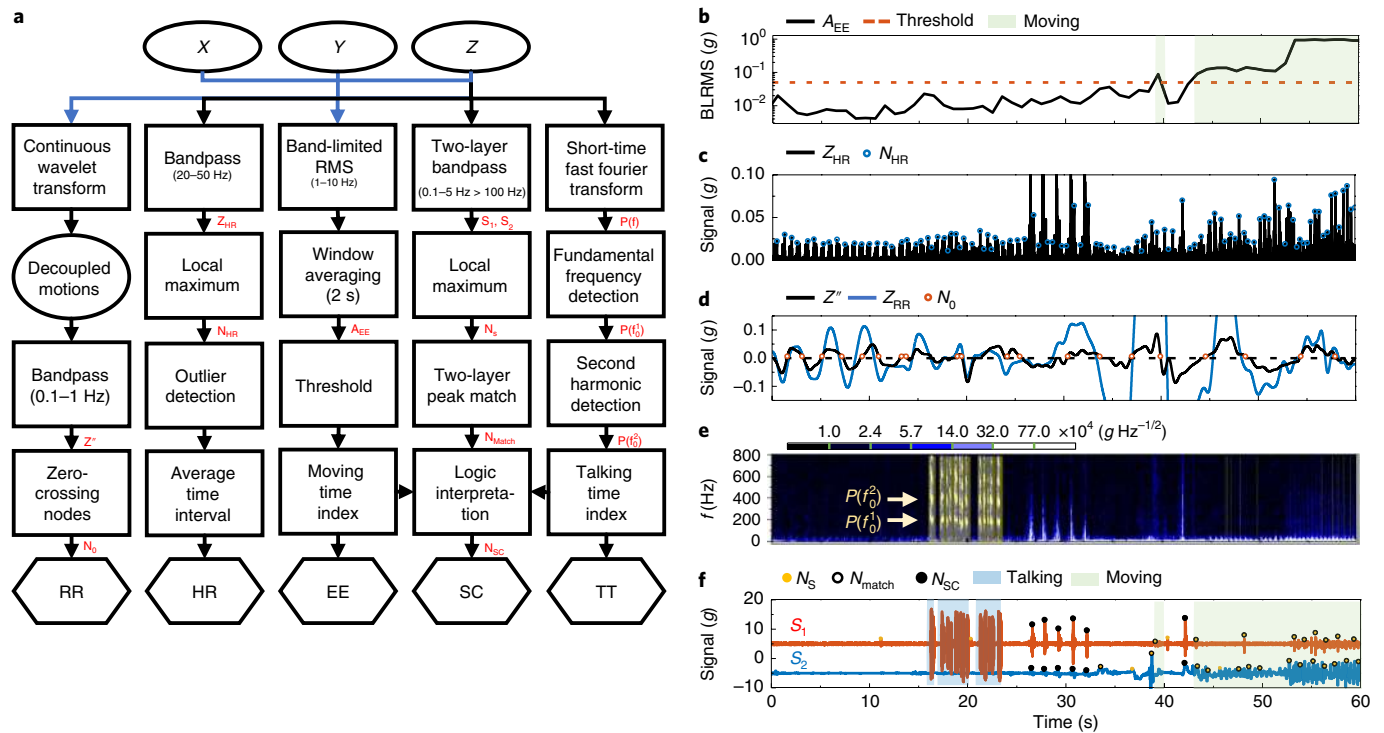


Fig. 3 | Flow diagram of signal processing and corresponding results from representative MA data acquired from healthy subjects. **a**, Block diagram of post-processing analytics for EE, HR, RR, SC and TT; blue arrows indicate use of three-axis accelerometer data and black arrows indicate use of z-axis data. EE, the window-averaged 1–10 Hz BLRMS sum of data from all three axes (A_{EE}) indicates the intensity of activities. For HR, detection of heartbeat peaks relies on identification of local maxima (N_{HR}) in 20–50 Hz band-passed waveforms (Z_{HR}). For RR, zero-crossing nodes (N_0) of the decoupled, 0.1–1 Hz band-passed chest wall motion (Z'') from three-axis measurements serve as the basis for RR estimation (Supplementary Note 3). For TT, the talking signals feature pronounced harmonics ($P(f_0^2)$ and $P(f_0^1)$) of fundamental frequencies (f_0^1) in the spectrogram analysis ($P(f)$). For SC, the broadband swallow-like events (N_{match}) correspond to occurrences of peaks (N_S) in both low-passed and high-passed signals ($S_1 = 0.1\text{--}5\text{ Hz}$; $S_2 > 100\text{ Hz}$). The algorithm outputs swallow-event N_{SC} that do not overlap with talking or activity periods. **b–f**, Application of the signal processing flow to the representative MA data (Fig. 2) for EE (**b**), HR (**c**), RR (**d**), TT and the colours indicating the amplitude spectral density (**e**) and SC (**f**) analysis.

The signals associated with each of these and other activities exhibit distinct features in time and frequency, thereby conveying a rich set of information related to body processes. The following analysis focuses, for simplicity, on accelerations measured along the direction normal to the surface of the skin (z axis).

The first 10 s of the data feature signals that arise from respiration. Here, expansion and contraction of the chest wall induce periodic rotations of the device around the y axis at the neck, along with some translational motions. The main effect is to change the magnitude of the projection of gravity along the z and x axes. Mounted on the SN, the device includes grounded points (for example, trachea) that do not move with the chest wall. Thus, the angular range of rotations ($\sim 1.3^\circ$) from respiration is larger than that associated with chest-wall movement alone ($\sim 0.5^\circ$). As the subject begins to hold his breath at the ~ 10 s mark, these periodic changes cease. Talking and swallowing generate high-frequency signals associated with acoustic vibrations and rapid motions, as shown in the data from 16–34 s. When the subject leans in different directions from 34–45 s, quasi-static 3D accelerations provide instantaneous measurements relative to the gravity vector indicative of body orientation. Walking (45–53 s) and jumping (53–60 s) induce large amplitude accelerations with significant projections along all axes.

Figure 2c shows quantitative details of the high-frequency features ($>10\text{ Hz}$) of individual physiological events. Cardiac activities—both systolic and diastolic¹⁰—give rise to paired pulses with peak amplitudes of $\sim 0.05\text{ g}$, and power concentrated in a frequency band of 20–50 Hz. The speech signals feature high-quality harmonic structures with fundamental frequencies in the range of

85 to 255 Hz for typical adults^{45,46}. Swallowing events initiate with slow motion ($\sim 0.1\text{ s}$) of the vocal folds and with larynx mechanics during the pharyngeal phase and end with a high-frequency ring-down associated with flow of water or food during the oesophageal stage⁶. Large impact forces that span broad frequency ranges up to $\sim 100\text{ Hz}$ characterize walking motions.

The characteristic frequencies and temporal structures of these features do not depend critically on the subject (gender, body type, ethnicity and age) (Supplementary Fig. 10) or the mounting location in the vicinity of the SN (Supplementary Fig. 11), although their relative amplitudes can vary slightly. For instance, the magnitudes of talking and swallowing signals increase as the mounting location approaches the larynx and upper oesophageal sphincter. The magnitudes of walking signals are invariant with position, as might be expected. Biological features across different subjects, including the fundamental frequencies of speech⁴⁷, the thickness of the skin and other aspects, lead to differences in the signal in ways that are expected and do not affect approaches in signal analysis and interpretation.

In practice, MA measurements consist of data streams that superpose physiological information from a multitude of sources. A processing flow that exploits the characteristic time-frequency features demonstrated in Fig. 2 enables separation of key events, each of relevance in medical and/or fitness monitoring, that is, energy expenditure (EE), heart rate (HR), respiration rate (RR), swallow counts (SC) and talking time (TT) (Fig. 3a).

Application of these strategies on the data in Fig. 2 demonstrates the scheme (Fig. 3b–f). Fig. 3b summarizes the EE over 2 s, with

a 50% overlapping moving-average window as a sum of all-axis low-frequency (1–10 Hz) band-limited root-mean square (BLRMS) data⁴⁸. The result enables classification of activity levels from low (sitting, $\sim 10^{-2}g$) to medium (walking, $\sim 10^{-1}g$) to high (jumping, $\sim 10^0g$) on a logarithmic scale.

Analysis of HR begins with the application of a bandpass filter ($f_{\text{low}} = 20 \text{ Hz}$, $f_{\text{high}} = 50 \text{ Hz}$; f_{low} and f_{high} are the low and high cut-off frequency, respectively) to the z -axis acceleration data to suppress noise outside the frequency range of interest. Cardiac pulses correspond to local maxima higher than $0.005g$ in the time series of these band-passed signals, ignoring intervals shorter than 0.33 s (~ 180 beats per minute (BPM)) and longer than 1.2 s (~ 50 BPM). Applying a 5 s , 50% overlapping moving window average to peak-to-peak intervals yields a running estimate of HR (Fig. 3c). The peak-detection algorithm, however, cannot operate reliably with motion artefacts that involve large impacts and associated temporal and spectral features that coincide with those due to comparatively subtle cardiac mechanics.

Measurements of RR are particularly sensitive to ambulatory signals due to overlaps of these two types of signals in the frequency domain (0.1–1 Hz). Traditional methods rely on three-axis accelerometers mounted on the chest or the abdomen and allow determination of RR only during periods that exclude effects of locomotion^{15,16,49}. Simple or weighted-sum methods (for example, principal component analysis) can make use of the multi-axis information¹⁷. In the approach reported here, a noise-subtraction algorithm exploits time-synchronized three-axis acceleration measurements to extract respiration signals at all activity levels. The detection mechanism relies critically on the SN mounting location and orientation (Fig. 1a,b), where the z -axis and x -axis measurements are both sensitive to chest wall motion, whereas the y -axis acceleration is mainly associated with core-body motions. A wavelet-transform projection yields common mode z' values between z - and x -axis measurements. The differential mode z'' between z' and y -axis measurements decouple motions from respiration. In each pair of projection, we retain wavelet transform coefficients with coherence larger than 0.8 (Supplementary Note 4).

Figure 3d compares the band-passed ($f_{\text{low}} = 0.1 \text{ Hz}$, $f_{\text{high}} = 1 \text{ Hz}$) z -axis measurement with z'' . Unlike traditional time-frequency analysis approaches for RR^{50,51}, a search for zero-crossing nodes of z'' determines the average time span of inspiration–expiration cycles \bar{T} in 1 min, as the basis for estimating RR as $60/\bar{T}$ BPM (Fig. 3d). The direct counting method accounts for the time non-stationary nature of respiration during physical activities. An adaptive threshold of 10% of the s.d. of the data helps reduce miscounting associated with small-amplitude and fast-ripple features on top of the overall 1-min respiration pattern (Fig. 3d and Supplementary Note 4).

Signals that arise from speech involve the prominent presence of a second harmonic of the fundamental frequency f_0^1 in the expected frequency range and magnitude (Fig. 3e). The talking time detected in this manner appears as shaded regions in Fig. 3e. Using our device to determine TT has distinct advantages over methods that rely on microphones due to its insensitivity to airborne acoustics. Tests in controlled, acoustically isolated rooms show that external sounds at 100 Hz and 90 dB(Z), appear as signals with amplitudes of only $2 \times 10^{-2}g \text{ Hz}^{-1/2}$ (Supplementary Fig. 12), whereas speech at a similar frequency and at 65 dB(Z) on microphone (near the audible threshold) appears on the device with maximum amplitude of $10^{-1}g \text{ Hz}^{-1/2}$ (Supplementary Fig. 13). The effects of ambient sounds can therefore be neglected entirely in almost all practical scenarios.

Swallowing events feature both low-frequency mechanical motions (0.1–5 Hz) and high-frequency acoustic components (100–800 Hz). On the basis of this observation, the algorithm for SC detects swallowing events as high-frequency and low-frequency peaks that occur, coincidentally, within a 2-s time window (Fig. 3f). For the purpose of this algorithm, swallowing events are only

considered if they are separated by more than 0.2 s from talking events and by more than 0.5 s from active periods (EE, $> 0.05g$).

Human subject evaluations in practical scenarios. Field studies in physical exercise and in dining demonstrate these data acquisition and processing schemes. The physical exercise study involves cycling and resting on a stationary bike, with HR between 50 to 180 BPM. A Polar hand-grip monitor yields reference HR values every 5 s (Fig. 4a). In a separate set of experiments, subjects manually count the number of breathing cycles per 5 min during normal sitting, walking and running activities as a reference for RR. For dining, each subject talks and swallows for 5 min according to a prescribed protocol. Here, periodicity (with a time scale of $\sim 10 \text{ s}$, significantly longer than the time scale of event detection of $\sim 0.1 \text{ s}$) in the activities facilitates tracking of numbers of events. In each minute of the n th test ($n = 0$ to 5), the subject talks for $n \times 10 \text{ s}$, then swallows at $(n + k) \times 10 \text{ s}$, where $k = 1$ to $6 - n$. During data acquisition, each subject marks the start and end of the talking period as well as swallowing instances using logging buttons on an app that runs on the smartphone used for data acquisition (Fig. 1d). The dataset includes five subjects for each scenario (Supplementary Table 1). For the cycling test, each subject cycles for 5 min. Applying a 5-s, zero-overlapping moving window generates a total of 301 samples for comparison. RR experiments yield 56 samples across different activity levels, wherein each sample is an average RR over one 5-min test. A total of 26 dining tests generate average values for TT and SC over each 5-min test.

Figure 4a–c shows example results of MA measurements versus reference data. In the exercise scheme, the MA HR follows the reference HR from 100 to 160 BPM over a time period of 5 min under cycling activity, as in Fig. 4a. In addition to HR, the MA device captures the amplitude of the cardiac activity, which exhibits an approximate linear correlation to HR. In Fig. 4b, the MA RR follows the manually counted RR for this 2-min segment during walking. The mean RR values in both cases, marked by the dashed lines, match closely. Figure 4c is a 1-min demonstration of the dining scheme. The MA talking and swallowing events agree with the label reference.

Figure 4d shows Bland–Altman plots for HR, RR, TT and SC. HR has a mean difference of 2.8 BPM and a s.d. of the difference between HR measurement and HR reference (A_{RMS}) of 6.5 BPM. This limit of agreement is comparable to that observed with some of the best commercial devices for HR monitoring during physical activity ($A_{\text{RMS}} = 4$ to 29 BPM). RR has a mean difference of 0.3 BPM and a s.d. of 2.5 BPM. As with HR, this difference is comparable to that of conventional monitors of RR ($A_{\text{RMS}} = 2$ to 3 BPM). A categorized statistical analysis indicates that the s.d. increases slightly with intensity of the activity (Supplementary Fig. 14). TT has a mean difference of -2.0 s min^{-1} and a s.d. of 2.2 s min^{-1} . SC has a mean difference of -0.7 counts per 5 min and a s.d. of 2.8 counts per 5 min.

Sleep studies. Use of MA devices to quantify patterns of sleep represents a potential application in advanced clinical diagnostics. Figure 5a shows a subject equipped with an MA device on the SN and with a complete suite of conventional polysomnography (PSG) sensors for gold-standard reference measurements. A sleep-laboratory technician performs visual observations alongside throughout the study to record changes in body orientation. In addition to HR and RR detection, the MA device also monitors quasi-static body orientation continuously, following calculations for a rotation matrix R that transforms gravity measurements in the canonical frame $g = (0, 0, -g_0)$ to the device frame $g' = (a_x, a_y, a_z)$, that is $g' = Rg$ (Supplementary Note 5).

Figure 5b shows an avatar representation of the subject in a left-recumbent position, along with the corresponding device and global frames of reference. The conversion of the rotation matrix to the Euler angles around the body-fixed (intrinsic) axis in z – y – x sequence (MATLAB function `rotm2eul`) better illustrates the

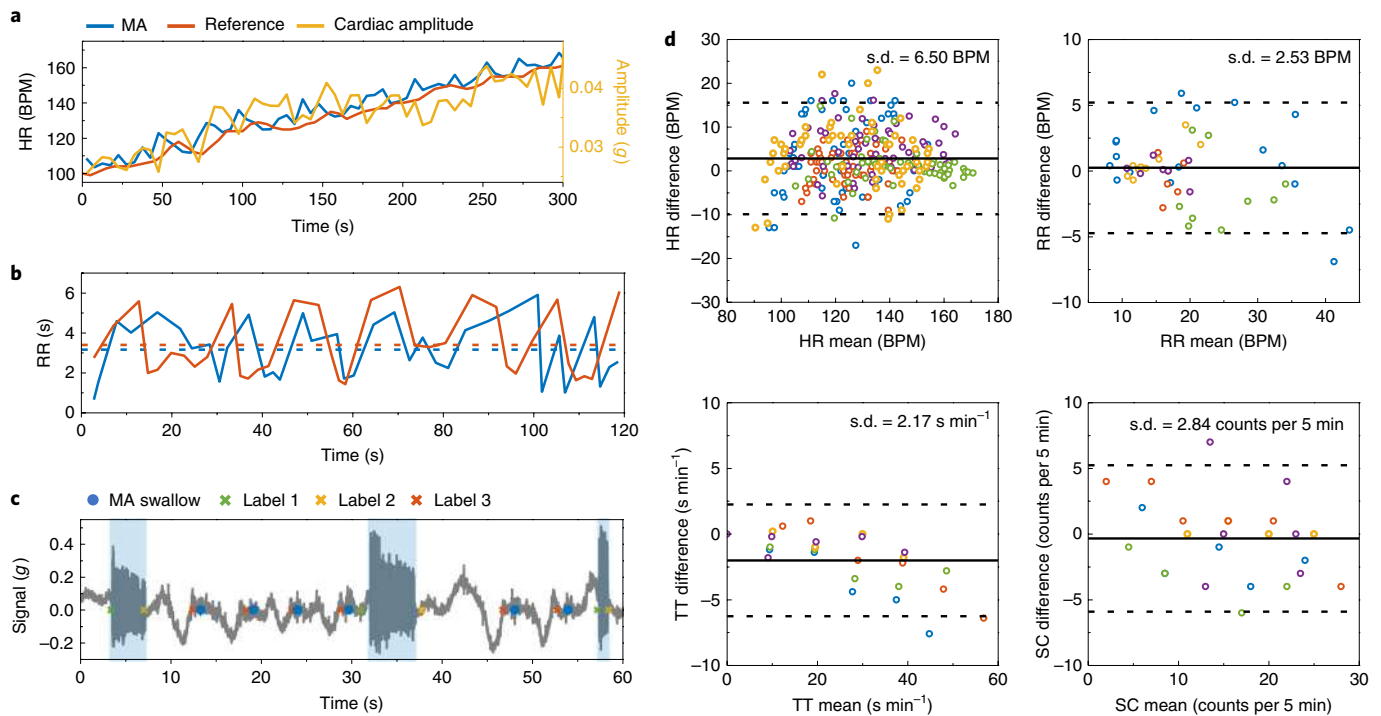


Fig. 4 | Results from MA data recorded at the SN in field studies with comparisons to reference measurements. **a**, HR measurements during a 5 min interval during exercise to increase the HR using MA signals and a Polar hand-grip monitor. The cardiac amplitude, measured as the peak acceleration amplitude, exhibits a correlation with the HR measurement. **b**, RR measurements during a 2 min interval using MA data and manual counting. The subject counts peak-to-peak intervals but the algorithm counts zero-to-zero intervals, thereby leading to a difference that appears as a time lag. **c**, A sample 1 min dining-scheme experiment comparing the reference labelling of events (cross) with the MA device detection (dot). Labels 1 and 2 mark the start and end of talking, respectively, while label 3 marks the occurrence of swallowing. **d**, The Bland-Altman analysis for HR, RR, TT and SC. The solid and dashed lines represent mean difference and $1.96 \times \text{s.d.}$ of the difference between MA measurements and reference values, respectively. Different colours represent the five healthy subjects.

rotation operation. The rotation angle θ around the longitudinal x axis characterizes the major body orientation of interest during sleep, where we define zero degree as supine and the positive sense as turning right (left-hand rule). Figure 5c presents a calibration test on rotation angles, in which a subject rolls into a series of body orientations. In addition to the supine, prone, left-recumbent and right-recumbent positions, the MA signal at the SN reveals additional information associated with the relative rotation of the head against the torso (Figs. 1a and 5c). Figure 5d–f compares HR measurements from MA devices with HR derived from electrocardiography (1-min window, 50% overlap), RR derived from PTAf (2-min window, 75% overlap) and sleep technician inspection measurements of body orientation (0.1-s window, 0% overlap) throughout a ~7-h sleep study on a healthy male (age 26, Korean) subject. Bland-Altman analysis for HR and RR gives a s.d. error of 3.9 BPM and 2.6 BPM, respectively (Supplementary Fig. 15).

As a routine part of clinical care, segments of sleep are classified into four different stages, excluding the wake stage. The duration and frequency of each stage determines the sleep quality. The four stages are rapid eye movement (REM), and non-REM stages N1, N2 and N3. REM sleep comprises irregular and high RR and HR, along with the large amplitude EOG signals recorded using the PSG suite⁵². Non-REM sleep stages are defined by characteristic features on EEG, and although the MA device does not record EEG or EOG data, the results in Fig. 5g suggest that it has some capabilities in quantifying sleep stages by applying machine learning algorithms on MA data obtained during stages determined manually by a clinical expert.

Here, a hidden Markov model determines sleep stages as generative sequences characterized by a set of observable sequences with an underlying probabilistic dependence (Supplementary Note 6).

The algorithm exploits multiband z -axis signal power on logarithmic scales as the observable clustering features, with a multiband choice featuring 0.1–0.8 Hz for respiration signals, sub-bands in the range 0.8–20 Hz for motions and 20–80 Hz for cardiac signals. As shown in Fig. 5g, the optimized inferred hidden states capture the overall trend of gold-standard sleep scoring. The success rate for a simple binary wake/asleep classification is 82%. Supplementary Fig. 16 includes a complete confusion matrix for multiclass. Advanced analytics, a subject of ongoing work, may enable further classification.

The wireless operation and the ability to track sleep with a single device facilitates use in home settings and in a way that does not alter natural patterns of sleep—significant advantages over PSG systems. Insights obtained in this way can guide behaviours to optimize sleep quality. For example, Fig. 6a shows the cumulative distribution function (CDF) of HR and RR statistics, extracted from data collected from eight healthy subjects over five nights of sleep in the home, classified into four body orientations (supine: $-45^\circ < \theta < 45^\circ$, left: $-135^\circ < \theta < -45^\circ$, right: $45^\circ < \theta < 135^\circ$, prone: $\theta > 135^\circ$ or $\theta < -135^\circ$). The solid lines are mean CDF values for all subjects. The shaded regions mark the s.d. variance between subjects (Fig. 6a). The inset compares the mean and s.d. of HR and RR respectively generated from the averaged CDF for different body orientations. The results indicate that the HR is highest, on average, in left-recumbent–prone–approximate positions. The RR is higher in recumbent positions but lower in prone positions, with supine as a reference. According to previous studies^{53–55}, such changes may relate to reductions in venous flow, with resulting blood pressure reductions and/or increases in reflexive sympathetic nervous activity.

As expected, the device is also sensitive to snoring signals. Figure 6b shows time-series and time-frequency analysis of a

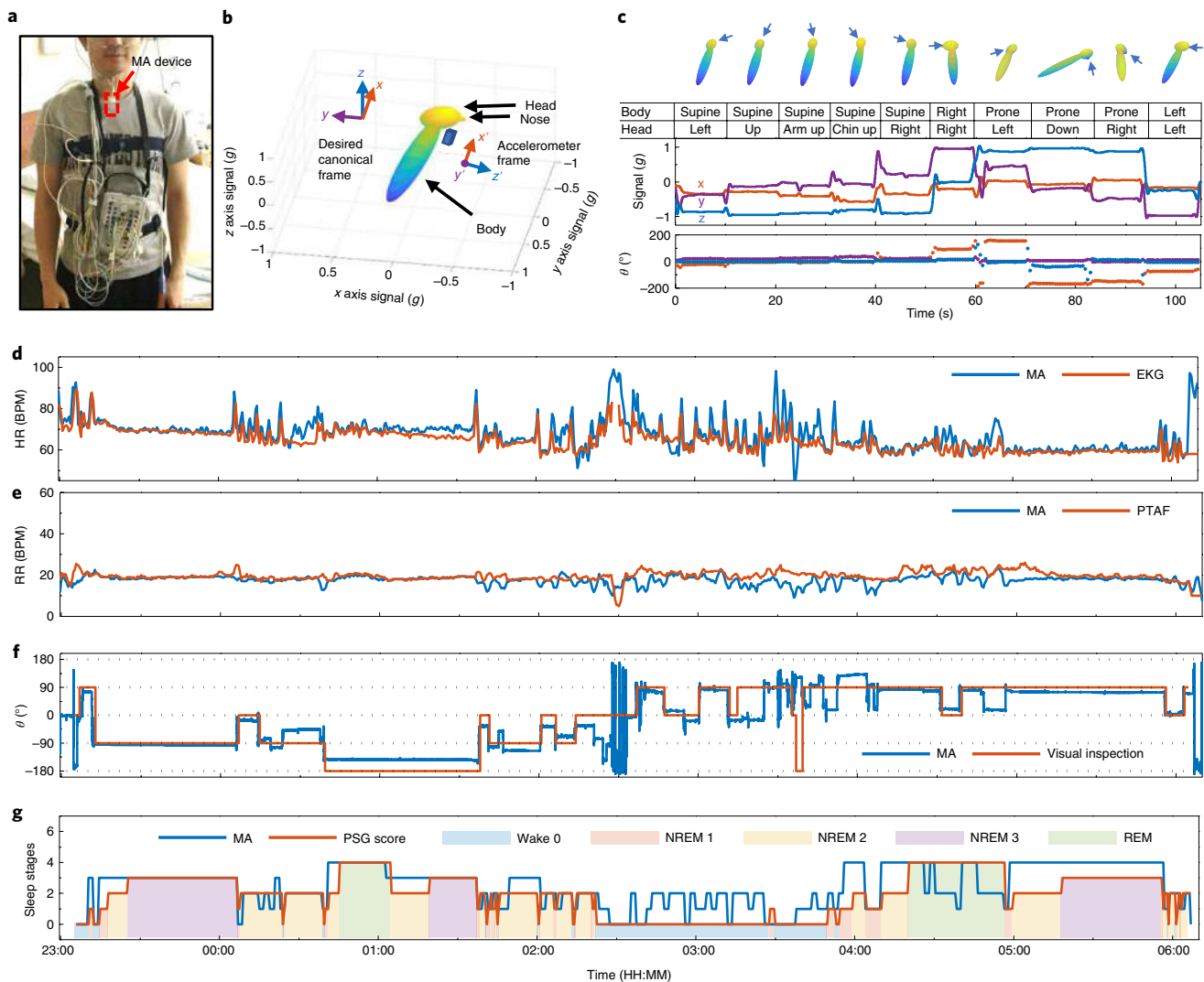


Fig. 5 | Application of MA sensing from the SN in clinical sleep studies. **a**, Image of the MA device on the SN (red box) along with a gold-standard PSG sensor ensemble, including devices for recording electrocardiograms (ECGs), electroencephalograms (EEGs) and electrooculograms (EOGs), and for pressure transducer air flow (PTAF) measurements, along with an abdomen strain gauge, thorax strain gauge and thermistor. **b**, Avatar representation of a subject with the associated device frame and canonical frame (colouring represents 3D rendering and is for illustrative purposes only). **c**, Body-orientation calibration test. The arrows indicate the position of the nose. **d**, Comparisons of HR determined with the MA sensor and with the ECG recordings during sleep. **e**, Comparisons of the RR determined with the MA sensor and with the nasal PTAF recordings during sleep. **f**, Comparisons of the body orientation determined with the MA sensor and by visual inspection by a sleep technician. **g**, Inference of sleep stages on the basis of multiband z-axis signal power of MA measurements compared with clinically determined sleep stages.

representative ~50 s period of snoring followed by a transition to a ~50 s period of quiet sleep from a healthy female subject. The time series superimposes the band-stopped ($f_{\text{low}} = 1 \text{ Hz}$, $f_{\text{high}} = 60 \text{ Hz}$) z-axis acceleration measurement with the band-passed ($f_{\text{low}} = 0.1 \text{ Hz}$, $f_{\text{high}} = 1 \text{ Hz}$) respiration signal, to show that snoring occurs during exhalation. The snoring-to-quiet transition in the sample of Fig. 6b correlates with a slight leftward head versus torso rotation of ~10°. The time-frequency analysis shows a clear presence of harmonics with fundamental frequency of ~50 Hz, which falls in the range of the natural frequencies of the soft palate and tongue structures^{56,57}. The TT algorithm can be adapted to search for snoring time (ST) by shifting the fundamental frequency search range to the lower frequencies ($20 \text{ Hz} < f_0^1 < 80 \text{ Hz}$). The auto-detected ST appears as shaded regions of the spectrogram plot. A tendency for snoring occurs during inspiration due to the Bernoulli effect⁵⁸. As the throat starts to narrow, the velocity of flow may increase which decreases the pressure in the airway behind the tongue and soft palate, thereby

drawing the tissues together. The timing relative to the inspiration period may indicate the anatomical origin of snoring: tongue, or soft palate. Figure 6c compares the snoring signal generated by these two different mechanisms. From 0 to 16 s, the subject artificially obstructs the airway by pushing the tongue to the back of the throat, then the subject artificially generates the snoring sound by vibrating the soft palate. The results clearly demonstrate that tongue snoring has inconsistent timing relative to the respiration cycle as compared to soft palate snoring. Moreover, the spectrogram illustrates that snoring generated by the tongue appears at a higher frequency range than that of the soft palate, as might be expected based on the mechanics of these processes.

Discussion

This paper summarizes a comprehensive set of concepts in hardware design and data analytics as the basis for an unusual class of soft, wireless MA sensor designed to operate on the SN, as a location

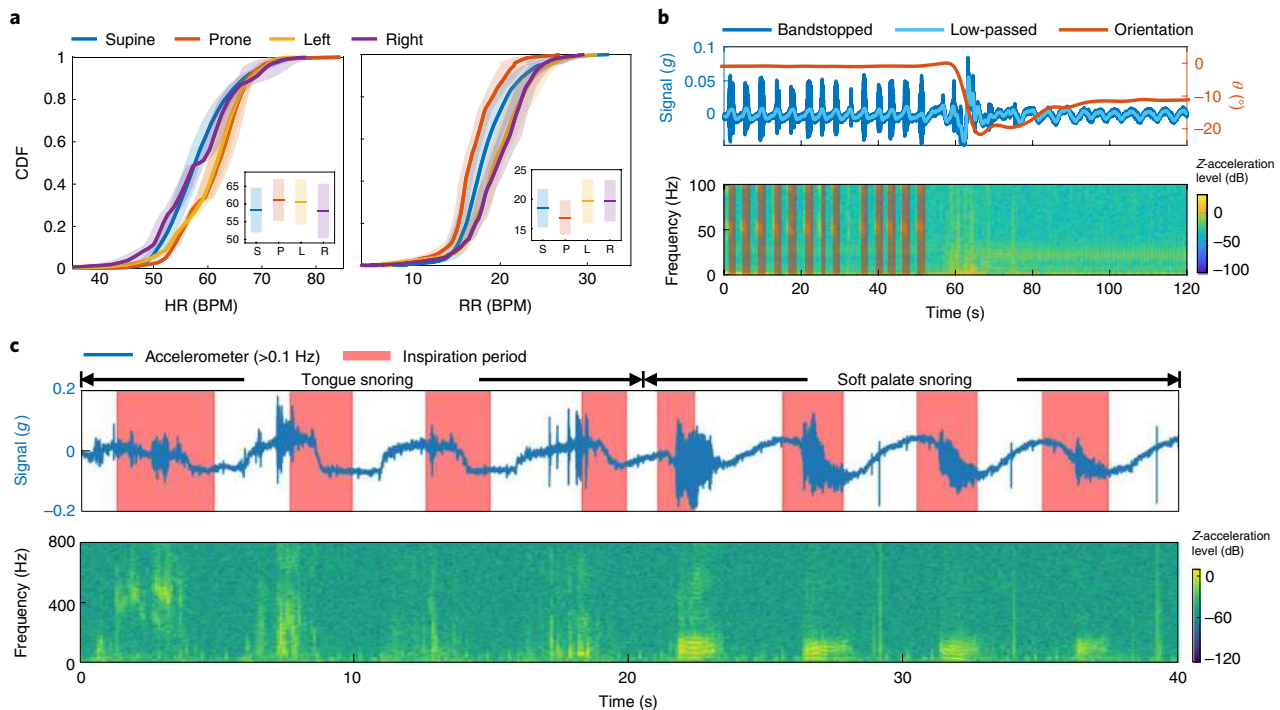


Fig. 6 | Insights into sleep patterns determined by MA sensing from the SN. **a**, CDF of HR and RR in supine (S), prone (P), left (L) and right (R) body orientations. Inset: indication of the mean (line) and s.d. (bars) of the measurements between subjects. **b**, Sample data that illustrate the transition from snoring to quiet periods, plotted along with body orientation. **c**, Comparisons of different types of snoring mechanisms and their characteristics in acceleration and frequency.

that enables collection of a unique set of multimodal data related to a range of physiological processes. Specific demonstrations in various practical scenarios show capabilities for simultaneously monitoring HR, TT, RR, SC and EE through data algorithms that exploit time- and frequency-domain representations, with additional possibilities in tracking body orientation, steps and gait, coughing events, respiratory sounds and many others. By design, the technologies and methods described here align well with current manufacturing practices and commercial components, thereby offering a high level of technology readiness. Increasing the range and sensitivity of the accelerometers and designing systems that incorporate multiple different types of accelerometers both have the potential to improve the functionality and expand the types of addressable applications.

Unresolved challenges for continuous monitoring include those that involve motion artefacts in cardiac signal and respiratory rate detection. Semi-continuous monitoring can, however, be accomplished by opportunistic sensing during times when such artefacts are absent¹⁴. Incorporating multinodal MA detection approaches represents an alternative route for signal decomposition and precise measurements of cardiac mechanics^{14,59}. The use of improved reference measurement methods in an ambulatory environment under intense and natural activities may aid in further development of data analytics approaches. Multimodal sensing enabled by the addition of strain gauges, for example, could enhance the accuracy in determining parameters, such as the respiration rate, that can be affected by low-frequency noise and motion artefacts. Evaluating signals under an expanded variety of daily activities with additional participants, improving analysis algorithms for enhanced performance and developing classification methods for a broader range of MA signals are interesting directions for future research.

The monitoring of sleep appears to be an important area of potential application, with significant advantages compared to both polysomnography systems and conventional wrist-mounted wearables. Others include uses in hospitals for monitoring

surgical recovery, particularly in paediatric populations, in assisted living environments to track social engagements, and in speech and physical therapy to treat aphasia and dysphagia. The straightforward addition of sensor modalities beyond accelerometry, such as pulse oximeters, could further expand the fields of use.

Methods

Fabrication of the electronics. Fabrication began with patterning a sheet of fPCB (12- μm -thick top and bottom Cu layer, 25- μm -thick middle polyimide layer, AP7164R, DuPont) into the necessary shapes using a ultraviolet laser cutter (LPKF U4). A CO₂ laser cutter (VLS3.50) defined pieces of FR4 board (0.381 mm, McMaster Carr 1331T37) into geometries matched to half of the sizes of the two electronic islands (Fig. 1b). Folding the island regions of the fPCB around the FR4 and bonding them in place using an adhesive (Loctite Tak Pak 444) yielded a dual-sided structure. Solder paste (Chip Quik TS391LT) joined the various electronic and sensor components onto the fPCB by reflow using a heat gun (AOYUE Int866).

Design of the encapsulating enclosure. A thin (~ 0.3 mm) elastomeric membrane of silicone (modulus, 60 kPa; toughness, 500 MPa) moulded into a preformed shape bonds on top of the planar silicone substrate around its perimeter to form a hollow enclosure that protects the system from the environment. This design provides a waterproof encapsulation structure that also allows free movement of the buckled serpentine interconnects (Supplementary Fig. 17). The device shows no degradation in performance after complete immersion in phosphate buffered saline solution at 70 °C for ten days. Compared with a conventional, solid-core encapsulation strategy, the hollow air-pocket layout reduces the equivalent tensile modulus, bending and twisting stiffness by ~ 3.4 , ~ 1.6 , and ~ 2.5 times, respectively (Supplementary Figs. 4 and 5d–f). Indeed, the equivalent tensile modulus is only ~ 18 kPa, nearly seven times lower than that of human skin (120 kPa)⁶⁰. The bending and twisting stiffnesses (~ 17.2 Nmm² and ~ 59.4 Nmm², respectively) are ~ 2.5 and ~ 3.9 times lower than those of the skin with comparable thickness.

A layer of a soft silicone gel (Silbione 4717 Gel A/B, Elkem) at the base of the system but within the encapsulating structure provides a degree of mechanical isolation from the underlying skin, where stresses would otherwise accumulate at the locations of the islands during motions and/or deformations of the body and skin. Simulations indicate that the shear and normal interfacial stresses remain below the threshold for sensation (~ 20 kPa) for deformations of the skin to tensile strains of up to 30% when the thickness of the gel is 400 μm (Supplementary Figs. 18 and 19). Without the strain-isolation layer, the stresses reach 20 kPa

at strains of only 10% (Supplementary Fig. 20). This strain-isolation layer does not, however, extend to the region of the device that supports the accelerometer, thereby ensuring its intimate mechanical coupling to the skin. The result enables high fidelity in MA measurements, as demonstrated by comparing data recorded using this device with those captured using the same accelerometer but in an isolated form connected by fine wires to external data acquisition electronics. Evaluations involve both systems on a vibrational stage or on a planar speaker, programmed to move in a sinusoidal manner with a frequency between 1 Hz to 100 Hz and between 100 Hz to 800 Hz, respectively (Supplementary Fig. 6). The measured responses are nearly identical in the frequency range of interest (0–800 Hz) except for a maximum of ~13% drop in the relative response around 91 Hz. Similar measurements show that the responses of the device are not significantly affected by stretching to tensile strains of 12% (Supplementary Fig. 21). Supplementary Fig. 7 summarizes an analytic model for the device on the skin (Supplementary Note 3). For frequencies between 1 and 50 Hz (Supplementary Fig. 8), the difference in the acceleration of skin with and without the device is less than 3%, due to the small mass (4.56 g) of the device.

Assembly of the device. A three-axis milling machine (Roland MDX 540) created aluminium moulds in geometries defined by three-dimensional computer-aided design drawings created using ProE Creo 3.0. The capping membrane was defined by casting a silicone thermoset polymer into the gap formed by matching pairs of moulds (Ecoflex, 00–30, smooth-on) with well controlled thickness (300 µm). Curing occurred in an oven at 70 °C for 15 min. The air cavity that enclosed the electronics was defined by bonding this membrane to a planar silicone substrate film around the perimeter.

Silicone gel (Silbione RT Gel 4717 A/B, Bluestar Silicone, Young's modulus (E) = 5 kPa) served as a strain-isolation layer at the base of the device. A manual screen-printing process delivered this material onto the substrate film in a pattern to match geometries of the islands. Heating on a hot plate at 100 °C for 5 min cured the gel. Fabrication was completed by delivering the electronics in aligned fashion onto this gel and capping the entire structure with the membrane.

Characterization of the device performance. Characterization focused on fully integrated devices and isolated accelerometers connected to external data acquisition electronics with fine wires (36 gauge). An acrylic silicone served as a bonding adhesive (3M, 2477p) to the centre of a speaker (JBL Go Portable 1) or to a vibration stage (3B Scientific) in both cases. The vibration stage and speaker were programmed to execute frequency sweeps from 1 to 100 Hz and from 100 to 800 Hz, respectively.

Data collection. The SN served as the mounting location in all cases. For the swallowing experiment, the duration of each session was 5 min. The subject talked and swallowed water for a prescribed number of times per minute throughout the session. The talking duration was 10 s per session, and the swallowing occurred every 10 s from the end of a previous talking session to the start of a subsequent one.

For the HR-monitoring session, the subject rode a cycling machine with a HR sensor interfaced to electrodes on the handle. The session began when the HR reached over 90 BPM. The subject cycled to increase the HR by 10 BPM each minute until reaching 170 BPM, as shown in the Fig. 4a.

For the sleep study, in addition to the MA device, the subject wore a suite of PSG sensors, including a three-channel system for EEG on the forehead, two channel leads for electrocardiography on the chest, a pair of leads for electromyography on the chin, a pair of channels for EOG on the side of upper left eye and lower right eye, a PTAF with thermistor in the nostrils and two strain-gauge bands around the chest and abdomen.

For all the studies, the participant gave informed consent.

Data analytics. All analysis used the MATLAB (R2018b) technical computing language. All digital manipulation uses a fourth order Butterworth infinite impulse response filter followed by a non-causal, zero-phase filtering approach (MATLAB function filtfilt). Identification of sleep stages used Python 3.0, with sci-kit learn and hmm learn packages.

Voice signal detection using harmonics. Given that $P(f_0^1)$ is a local maximum of power spectral density $P(f)$ in the range of the human voice ($f_0^1 < 160$ Hz for male subjects, $150 \text{ Hz} < f_0^1 < 400$ Hz for female subjects) (Fig. 3e), the algorithm searches for a local maximum $P(f_0^2)$ in the frequency range $\frac{3}{2}f_0^1 < f_0^2 < \frac{5}{2}f_0^1$ and identifies speech if the search matches the anticipated harmonics behaviour within a tolerance distance $|f_0^2 - 2f_0^1| \leq 10 \text{ Hz}$. Instances with $f_0^2 < 120$ Hz and $P(f_0^2) < 5 \times 10^{-3} \text{ g Hz}^{-1/2}$ are not considered.

Classifying active and inactive states. Identification of active versus inactive states uses a fixed threshold of $0.05 \text{ g} = \bar{s} + 5\delta s$, where s is the first 30 s of EE measurement as the subject sits quietly with minor movements, and $\bar{s} \approx 0.012 \text{ g}$ and $\delta s \approx 0.008 \text{ g}$ are the characteristic mean and s.d. of s .

Mechanics of swallow-event detection. This criterion allows for only one high-frequency peak to be paired with the temporally closest low-frequency peak. Evaluating the stochastic differential of the signal zeros the quasi-static offset before the data pass through the low-pass filter. The algorithm then locates

local maxima in the resulting time series of minimum peak prominences of $5 \times 10^{-4} \text{ g}$, a minimum peak distance of 1 s and a maximum peak width at half maximum of 0.5 s. High-passed peaks are detected with a minimum peak height of $0.024 \text{ g} \approx 5A_{\text{BLRMS}}$, where A_{BLRMS} is the high-frequency (100–800 Hz) BLRMS of quiet-time signals.

Reporting Summary. Further information on research design is available in the Nature Research Reporting Summary linked to this article.

Data availability

The main data supporting the results in this study are available within the paper and its Supplementary Information. The raw and analysed datasets generated for the studies in Figs. 2–6 are available for research purposes from the corresponding authors upon reasonable request.

Code availability

The codes used for the embedded system and data collection are available on GitHub at https://github.com/johnrogersgroup/Wireless_MA. The analysis codes used in this study are available from the authors upon request.

Received: 3 June 2019; Accepted: 11 October 2019;

Published online: 25 November 2019

References

- Liu, Y. et al. Epidermal mechano-acoustic sensing electronics for cardiovascular diagnostics and human-machine interfaces. *Sci. Adv.* **2**, e1601185 (2016).
- Kaniusas, E. in *Biomedical Signals and Sensors II: Linking Acoustic and Optic Biosignals and Biomedical Sensors* (Springer, 2015).
- Hu, Y., Kim, E. G., Cao, G., Liu, S. & Xu, Y. Physiological acoustic sensing based on accelerometers: a survey for mobile healthcare. *Ann. Biomed. Eng.* **42**, 2264–2277 (2014).
- Vavrinský, E. et al. Application of acceleration sensors in physiological experiments. *J. Electr. Eng.* **65**, 304–308 (2014).
- Makarenkova, A., Poreva, A. & Slozko, M. Efficiency evaluation of electroacoustic sensors for auscultation devices of human body life-activity sounds. In *Proc. IEEE 1st Ukraine Conference on Electrical and Computer Engineering* (IEEE, 2017).
- Dudík, J. M., Coyle, J. L. & Sejdíć, E. Dysphagia screening: contributions of cervical auscultation signals and modern signal-processing. *Tech. IEEE Trans. Hum. Mach. Syst.* **45**, 465–477 (2015).
- Kok, M., Hol, J. D. & Schön, T. B. Using inertial sensors for position and orientation estimation. *Found. Trends Signal Process.* **11**, 1–153 (2017).
- Makaryus, A. N., Swarup, S. & Makaryus, A. Digital stethoscope: technology update. *Med. Devices* **11**, 29–36 (2018).
- Brond, J. C. & Arvidsson, D. Sampling frequency affects the processing of Actigraph raw acceleration data to activity counts. *J. Appl. Physiol.* **120**, 362–369 (2016).
- Di Rienzo, M. et al. A wearable system for the seismocardiogram assessment in daily life conditions. In *Proc. Annual International Conference of the IEEE Engineering in Medicine and Biology Society* (IEEE, 2011).
- Jafari Tadi, M. et al. Gyrocardiography: A new non-invasive monitoring method for the assessment of cardiac mechanics and the estimation of hemodynamic variables. *Sci. Rep.* **7**, 1–11 (2017).
- Inan, O. T. et al. Novel wearable seismocardiography and machine learning algorithms can assess clinical status of heart failure patients. *Circ. Heart Fail.* **11**, e004313 (2018).
- Shandhi, M. M. H. et al. Performance analysis of gyroscope and accelerometer sensors for seismocardiography-based wearable pre-ejection period estimation. *IEEE J. Biomed. Health* **23**, 2365–2374 (2019).
- Hernandez, J., McDuff, D., Quigley, K. S., Maes, P. & Picard, R. W. Wearable motion-based heart-rate at rest: a workplace evaluation. *IEEE J. Biomed. Health* **23**, 1920–1927 (2019).
- Hung, P. D., Bonnet, S., Guillemaud, R., Castelli, E. & Yen, P. T. N. Estimation of respiratory waveform using an accelerometer. In *Proc. 5th IEEE International Symposium on Biomedical Imaging: From Nano to Macro* (IEEE, 2008).
- Bates, A., Ling, M. J., Mann, J. & Arvind, D. K. Respiratory rate and flow waveform estimation from tri-axial accelerometer data. In *Proc. 2010 International Conference on Body Sensor Networks* (IEEE, 2010).
- Liu, G. Z., Guo, Y. W., Zhu, Q. S., Huang, B. Y. & Wang, L. Estimation of respiration rate from three-dimensional acceleration data based on body sensor network. *Telemed. J. E. Health* **17**, 705–711 (2011).
- Lapi, S. et al. Respiratory rate assessments using a dual-accelerometer device. *Respir. Physiol. Neurobiol.* **191**, 60–66 (2014).
- Tadi, M. J. et al. A miniaturized MEMS motion processing system for nuclear medicine imaging applications. *Comput. Cardiol.* **43**, 133–136 (2016).

20. Preejith, S. P., Jeelani, A., Maniyar, P., Joseph, J. & Sivaprakasam, M. Accelerometer based system for continuous respiratory rate monitoring. In *Proc. IEEE International Symposium on Medical Measurements and Applications* (IEEE, 2017).
21. Pompilio, P. P., Sgura, A., Pedotti, A. & Dellaca, R. A MEMS accelerometers based system for the measurement of lung sound delays. In *Proc. 5th Cairo International Biomedical Engineering Conference* (IEEE, 2010).
22. Lee, J., Steele, C. M. & Chau, T. Time and time-frequency characterization of dual-axis swallowing accelerometry signals. *Physiol. Meas.* **29**, 1105–1120 (2008).
23. Damouras, S., Sejdíć, E., Steele, C. M. & Chau, T. An online swallow detection algorithm based on the quadratic variation of dual-axis accelerometry. *IEEE Trans. Signal Process.* **58**, 3352–3359 (2010).
24. Dudík, J. M., Jestrović, I., Luan, B., Coyle, J. L. & Sejdíć, E. A comparative analysis of swallowing accelerometry and sounds during saliva swallows. *Biomed. Eng. Online* **14**, 3 (2015).
25. Kumari, S. K. & Mathana, J. M. Blood sugar level indication through chewing and swallowing from acoustic MEMS sensor and deep learning algorithm for diabetic management. *J. Med. Syst.* **43**, 1 (2018).
26. Mehta, D. D., Zaňartu, M., Feng, S. W., Cheyne, H. A. I. & Hillman, R. E. Mobile voice health monitoring using a wearable accelerometer sensor and a smartphone platform. *IEEE Trans. Biomed. Eng.* **59**, 3090–3096 (2012).
27. Michalevsky, Y., Boneh, D. & Nakibly, G. Gyrophone: recognizing speech from gyroscope signals. In *Proc. 23rd USENIX Security Symposium* (USENIX Association, 2014).
28. Nyan, M. N., Tay, F. E. H., Manimaran, M. & Seah, K. H. W. Garment-based detection of falls and activities of daily living using 3-axis MEMS accelerometer. *J. Phys. Conf. Ser.* **34**, 1059–1067 (2006).
29. Curone, D., Bertolotti, G. M., Cristiani, A., Secco, E. L. & Magenes, G. A real-time and self-calibrating algorithm based on triaxial accelerometer signals for the detection of human posture and activity. *IEEE Trans. Inf. Technol. Biomed.* **14**, 1098–1105 (2010).
30. Yang, C. C. & Hsu, Y. L. A review of accelerometry-based wearable motion detectors for physical activity monitoring. *Sensors* **10**, 7772–7788 (2010).
31. Posatskiy, A. O. & Chau, T. The effects of motion artifact on mechanomyography: A comparative study of microphones and accelerometers. *J. Electromyogr. Kinesiol.* **22**, 320–324 (2012).
32. Maki, H., Ogawa, H., Matsuoka, S., Yonezawa, Y. & Caldwell, W. M. A daily living activity remote monitoring system for solitary elderly people. *Proc. Annu. Int. Conf. IEEE Eng. Med. Biol. Soc. EMBS* **2011**, 5608–5611 (2011).
33. Zheng, Y. L. et al. Unobtrusive sensing and wearable devices for health informatics. *IEEE Trans. Biomed. Eng.* **61**, 1538–1554 (2014).
34. Phan, D. H., Bonnet, S., Guillemaud, R., Castelli, E. & Thi, N. Y. P. Estimation of respiratory waveform and heart rate using an accelerometer. In *Proc. 30th Annual International Conference of the IEEE Engineering in Medicine and Biology Society* (IEEE, 2008).
35. Vertens, J. et al. Measuring respiration and heart rate using two acceleration sensors on a fully embedded platform. In *Proc. 3rd International Congress on Sport Sciences Research and Technology Support* (Scitepress, 2015).
36. Sánchez Morillo, D., Ojeda, J. L. R., Foix, L. F. C. & Jiménez, A. L. An accelerometer-based device for sleep apnea screening. *IEEE Trans. Inf. Technol. Biomed.* **14**, 491–499 (2010).
37. He, D. Da, Winokur, E. S. & Sodini, C. G. An ear-worn continuous ballistocardiogram (BCG) sensor for cardiovascular monitoring. *Conf. Proc. IEEE Eng. Med. Biol. Soc.* **2012**, 5030–5033 (2012).
38. Rahman, T. et al. BodyBeat: a mobile system for sensing non-speech body sounds. In *Proc. 12th Annual International Conference on Mobile Systems, Applications, and Services* (ACM, 2014).
39. Kim, D. H. et al. Epidermal electronics. *Science* **333**, 838–843 (2011).
40. Jang, K. I. et al. Soft network composite materials with deterministic and bio-inspired designs. *Nat. Commun.* **6**, 6566 (2015).
41. Fan, J. A. et al. Fractal design concepts for stretchable electronics. *Nat. Commun.* **5**, 3266 (2014).
42. Kim, D. H. et al. Electronic sensor and actuator webs for large-area complex geometry cardiac mapping and therapy. *Proc. Natl Acad. Sci. USA* **109**, 19910–19915 (2012).
43. Kim, D. H. et al. Materials and noncoplanar mesh designs for integrated circuits with linear elastic responses to extreme mechanical deformations. *Proc. Natl Acad. Sci. USA* **105**, 18675–18680 (2008).
44. Muroga, T., Ito, Y., Aoyagi, K., Yamamoto, Y. & Yokomizo, K. Rolled copper foil. US patent 20090017325A1 (2009).
45. Titze, I. R. *Principles of Voice Production* (Prentice Hall, 1994).
46. Baken, R. J. & Orlikoff, R. F. *Clinical measurement of speech and voice* (Cengage Learning, 1999).
47. Wu, K. Gender recognition from speech. Part II: fine analysis. *J. Acoust. Soc. Am.* **90**, 1841–1856 (1991).
48. Lin, S. J. et al. A pilot study on BSN-based ubiquitous energy expenditure monitoring. In *Proc. 6th International Workshop on Wearable and Implantable Body Sensor Networks* (IEEE, 2009).
49. Jin, A., Yin, B., Morren, G., Duric, H. & Aarts, R. M. Performance evaluation of a tri-axial accelerometry-based respiration monitoring for ambient assisted living. In *Proc. 31st Annual International Conference of the IEEE Engineering in Medicine and Biology Society: Engineering the Future of Biomedicine* (IEEE, 2009).
50. Dash, S., Shelley, K. H., Silverman, D. G. & Chon, K. H. Estimation of respiratory rate from ECG, photoplethysmogram, and piezoelectric pulse transducer signals: a comparative study of time-frequency methods. *IEEE Trans. Biomed. Eng.* **57**, 1099–1107 (2010).
51. Chon, K. H., Dash, S. & Ju, K. Estimation of respiratory rate from photoplethysmogram data using time-frequency spectral estimation. *IEEE Trans. Biomed. Eng.* **56**, 2054–2063 (2009).
52. Berry, R. B. et al. AASM scoring manual updates for 2017 (version 2.4). *J. Clin. Sleep Med.* **13**, 665–666 (2017).
53. Watanabe, N., Reece, J. & Polus, B. I. Effects of body position on autonomic regulation of cardiovascular function in young, healthy adults. *Chiropr. Osteopat.* **15**, 19 (2007).
54. Toyota, S. & Amaki, Y. Hemodynamic evaluation of the prone position by transesophageal echocardiography. *J. Clin. Anesth.* **10**, 32–35 (1998).
55. Pump, B., Tolleruphuus, U., Christensen, N. J., Warberg, J. & Norsk, P. Effects of supine, prone, and lateral positions on cardiovascular and renal variables in humans. *Am. J. Physiol.* **283**, R174–R180 (2002).
56. Issa, F. G. & Sullivan, C. E. Upper airway closing pressures in snorers. *J. Appl. Physiol.* **57**, 528–535 (1984).
57. Aurégan, Y. & Depollier, C. Snoring: linear stability analysis and in-vitro experiments. *J. Sound Vib.* **188**, 39–53 (1995).
58. Fajdiga, I. Snoring imaging: could Bernoulli explain it all? *Chest* **128**, 896–901 (2005).
59. Javadi, A. Q. et al. Quantifying and reducing motion artifacts in wearable seismocardiogram measurements during walking to assess left ventricular health. *IEEE Trans. Biomed. Eng.* **64**, 1277–1286 (2017).
60. Schwindt, D. A., Wilhelm, K. P., Miller, D. L. & Maibach, H. I. Cumulative irritation in older and younger skin: a comparison. *Acta Derm. Venereol.* **78**, 279–283 (1998).

Acknowledgements

The materials and device-engineering aspects of the research were supported by the Material Science and Engineering Department and Center for Bio-Integrated Electronics at Northwestern University. K.L. acknowledges support from the Samsung Scholarship. K.L. acknowledges the help from A. Sahakian on radio frequency communication and antenna tuning. Z.X. acknowledges support from the National Natural Science Foundation of China (grant no.11402134). S.X. and J.A.R. recognizes support from the National Institute on Aging of the National Institutes of Health under R41AG062023 and R43AG060812. R.A. acknowledges support from National Science Foundation (NSF) Graduate Research Fellowship under grant no. 1842165 and the Ford Foundation Predoctoral Fellowship. Y.H. acknowledges support from the NSF (CMMI1635443). S.M. is grateful to Indo-U.S. Science and Technology Forum (SERB-IUSSTF) for her SERB Indo-U.S. Postdoctoral Award. X.N. thanks D. Lu for helpful discussions. K.L. thanks the Dion family for volunteering for the data collection.

Author contributions

K.L., Z.X. and J.A.R. performed the structural design of the system. Z.X., R.A., Y.D. and Y.H. performed mechanical and electromagnetic modelling and theoretical studies. K.L., J.Y.L., J.H.L., J.B.P. and J.K. developed the embedded system and the user interface. K.L., X.N. and J.A.R. designed and performed the experimental studies on the technology. X.N., K.L. and J.A.R. designed and performed the human subject studies. X.N., K.L., M.I., R.L.E., D.J.P. and D.H.K. developed the signal-processing algorithms and performed the data analysis. K.L., H.A., D.J.P., H.U.C., O.O.O., S.G., E.C., M.H., J.B., H.J., C.L., S.B.K., S.M., J.T.R. and I.H. manufactured the devices. S.X., A.T. and C.R.D. provided clinical advice. X.N. and J.A.R. wrote the signal processing algorithm part of the manuscript. K.L., X.N., Z.X., Y.H. and J.A.R. contributed to the other sections.

Competing interests

The authors declare no competing interests.

Additional information

Supplementary information is available for this paper at <https://doi.org/10.1038/s41551-019-0480-6>.

Correspondence and requests for materials should be addressed to Z.X., C.R.D., Y.H. or J.A.R.

Reprints and permissions information is available at www.nature.com/reprints.

Publisher's note Springer Nature remains neutral with regard to jurisdictional claims in published maps and institutional affiliations.

© The Author(s), under exclusive licence to Springer Nature Limited 2019

Reporting Summary

Nature Research wishes to improve the reproducibility of the work that we publish. This form provides structure for consistency and transparency in reporting. For further information on Nature Research policies, see [Authors & Referees](#) and the [Editorial Policy Checklist](#).

Statistics

For all statistical analyses, confirm that the following items are present in the figure legend, table legend, main text, or Methods section.

- | | |
|-------------------------------------|--|
| n/a | Confirmed |
| <input type="checkbox"/> | <input checked="" type="checkbox"/> The exact sample size (n) for each experimental group/condition, given as a discrete number and unit of measurement |
| <input type="checkbox"/> | <input checked="" type="checkbox"/> A statement on whether measurements were taken from distinct samples or whether the same sample was measured repeatedly |
| <input type="checkbox"/> | <input checked="" type="checkbox"/> The statistical test(s) used AND whether they are one- or two-sided
<i>Only common tests should be described solely by name; describe more complex techniques in the Methods section.</i> |
| <input type="checkbox"/> | <input checked="" type="checkbox"/> A description of all covariates tested |
| <input type="checkbox"/> | <input checked="" type="checkbox"/> A description of any assumptions or corrections, such as tests of normality and adjustment for multiple comparisons |
| <input type="checkbox"/> | <input checked="" type="checkbox"/> A full description of the statistical parameters including central tendency (e.g. means) or other basic estimates (e.g. regression coefficient) AND variation (e.g. standard deviation) or associated estimates of uncertainty (e.g. confidence intervals) |
| <input checked="" type="checkbox"/> | <input type="checkbox"/> For null hypothesis testing, the test statistic (e.g. F , t , r) with confidence intervals, effect sizes, degrees of freedom and P value noted
<i>Give P values as exact values whenever suitable.</i> |
| <input type="checkbox"/> | <input checked="" type="checkbox"/> For Bayesian analysis, information on the choice of priors and Markov chain Monte Carlo settings |
| <input checked="" type="checkbox"/> | <input type="checkbox"/> For hierarchical and complex designs, identification of the appropriate level for tests and full reporting of outcomes |
| <input checked="" type="checkbox"/> | <input type="checkbox"/> Estimates of effect sizes (e.g. Cohen's d , Pearson's r), indicating how they were calculated |

Our web collection on [statistics for biologists](#) contains articles on many of the points above.

Software and code

Policy information about [availability of computer code](#)

Data collection: Custom Android application; custom iOS application; custom embedded code; Sandman 10.1.

Data analysis: Custom MATLAB and Python code (MATLAB 2018b; Python 3.0).

For manuscripts utilizing custom algorithms or software that are central to the research but not yet described in published literature, software must be made available to editors/reviewers. We strongly encourage code deposition in a community repository (e.g. GitHub). See the Nature Research [guidelines for submitting code & software](#) for further information.

Data

Policy information about [availability of data](#)

All manuscripts must include a [data availability statement](#). This statement should provide the following information, where applicable:

- Accession codes, unique identifiers, or web links for publicly available datasets
- A list of figures that have associated raw data
- A description of any restrictions on data availability

The main data supporting the results in this study are available within the paper and its Supplementary Information. The raw and analysed datasets generated for the studies in Figs. 2–6 are available for research purposes from the corresponding authors on reasonable request.

Field-specific reporting

Please select the one below that is the best fit for your research. If you are not sure, read the appropriate sections before making your selection.

- ☒ Life sciences ☐ Behavioural & social sciences ☐ Ecological, evolutionary & environmental sciences

Life sciences study design

All studies must disclose on these points even when the disclosure is negative.

Sample size	No sample size calculation was performed. A sample size of 5 provides sufficient information on the repeatability of different types of mechanical and vibratory signals.
Data exclusions	No data were excluded from the analyses.
Replication	The mechanoacoustic recordings were repeated more than ten times. The results were replicable, and any small discrepancy in the data were displayed explicitly.
Randomization	All devices tested were selected randomly.
Blinding	The investigators were blinded to group allocation during data collection and analysis.

Reporting for specific materials, systems and methods

We require information from authors about some types of materials, experimental systems and methods used in many studies. Here, indicate whether each material, system or method listed is relevant to your study. If you are not sure if a list item applies to your research, read the appropriate section before selecting a response.

Materials & experimental systems

Methods

n/a	Involved in the study	n/a	Involved in the study
<input checked="" type="checkbox"/>	<input type="checkbox"/> Antibodies	<input checked="" type="checkbox"/>	<input type="checkbox"/> ChIP-seq
<input checked="" type="checkbox"/>	<input type="checkbox"/> Eukaryotic cell lines	<input checked="" type="checkbox"/>	<input type="checkbox"/> Flow cytometry
<input checked="" type="checkbox"/>	<input type="checkbox"/> Palaeontology	<input checked="" type="checkbox"/>	<input type="checkbox"/> MRI-based neuroimaging
<input checked="" type="checkbox"/>	<input type="checkbox"/> Animals and other organisms		
<input type="checkbox"/>	<input checked="" type="checkbox"/> Human research participants		
<input checked="" type="checkbox"/>	<input type="checkbox"/> Clinical data		

Human research participants

Policy information about [studies involving human research participants](#)

Population characteristics	Participants in the experiments were healthy subjects.
Recruitment	The participants were recruited by the Materials Science and Engineering and Biomedical Engineering at Northwestern University. The participants for the sleep study were two of the investigators, who volunteered to be subjects. There were no self-selection biases or other biases.
Ethics oversight	Human-subject participation was entirely voluntary. The devices used are considered to carry minimal risk, and therefore approval was not needed.

Note that full information on the approval of the study protocol must also be provided in the manuscript.

In the format provided by the authors and unedited.

Mechano-acoustic sensing of physiological processes and body motions via a soft wireless device placed at the suprasternal notch

KunHyuck Lee^{1,2,21}, Xiaoyue Ni^{3,21}, Jong Yoon Lee^{3,21}, Hany Arafa^{1,4}, David J. Pe⁵, Shuai Xu^{1,3,6}, Raudel Avila^{2,3,7,8}, Masahiro Irie^{1,9}, Joo Hee Lee³, Ryder L. Easterlin¹⁰, Dong Hyun Kim¹¹, Ha Uk Chung^{1,9}, Omolara O. Olabisi⁴, Selam Getaneh⁸, Esther Chung⁴, Marc Hill⁴, Jeremy Bell¹², Hokyung Jang³, Claire Liu^{1,4}, Jun Bin Park¹³, Jungwoo Kim³, Sung Bong Kim¹⁴, Sunita Mehta³, Matt Pharr¹⁵, Andreas Tzavelis¹⁶, Jonathan T. Reeder^{2,3}, Ivy Huang^{1,2}, Yujun Deng^{2,3,7,8,17}, Zhaoqian Xie^{2,3,7,8,18*}, Charles R. Davies^{19*}, Yonggang Huang^{2,3,7,8*} and John A. Rogers^{1,2,3,4,5,8,9,20*}

¹Simpson Querry Institute, Northwestern University, Chicago, IL, USA. ²Department of Materials Science and Engineering, Northwestern University, Evanston, IL, USA. ³Center for Bio-Integrated Electronics, Northwestern University, Evanston, IL, USA. ⁴Department of Biomedical Engineering, Northwestern University, Evanston, IL, USA. ⁵Department of Chemistry, Northwestern University, Evanston, IL, USA. ⁶Department of Dermatology, Feinberg School of Medicine, Northwestern University, Chicago, IL, USA. ⁷Department of Civil and Environmental Engineering, Northwestern University, Evanston, IL, USA. ⁸Department of Mechanical Engineering, Northwestern University, Evanston, IL, USA. ⁹Department of Electrical and Computer Engineering, Northwestern University, Evanston, IL, USA. ¹⁰Department of Molecular Biosciences, Northwestern University, Evanston, IL, USA. ¹¹Department of Electrical and Computer Engineering, University of Illinois at Urbana-Champaign, Urbana, IL, USA. ¹²Department of Economics, Northwestern University, Evanston, IL, USA. ¹³Department of Statistics, University of Illinois at Urbana-Champaign, Urbana, IL, USA. ¹⁴Department of Materials Science and Engineering, University of Illinois at Urbana-Champaign, Urbana, IL, USA. ¹⁵Department of Mechanical Engineering, Texas A&M University, College Station, TX, USA. ¹⁶Medical Scientist Training Program, Feinberg School of Medicine, Northwestern University, Chicago, IL, USA. ¹⁷State Key Laboratory of Mechanical System and Vibration, Shanghai Jiao Tong University, Shanghai, China. ¹⁸State Key Laboratory of Structural Analysis for Industrial Equipment, Department of Engineering Mechanics, Dalian University of Technology, Dalian, China. ¹⁹Carle Neuroscience Institute, Carle Physician Group, Urbana, IL, USA. ²⁰Department of Neurological Surgery, Northwestern University, Evanston, IL, USA. ²¹These authors contributed equally: KunHyuck Lee, Xiaoyue Ni, Jong Yoon Lee. *e-mail: xiezhaoqian@gmail.com; charles.davies@carle.com; y-huang@northwestern.edu; jrogers@northwestern.edu

Supplementary Information

Note S1.	System Operation Flow	2
Note S2.	Finite element analysis	2
Note S3.	The theoretical vibration model of a one-dimensional rod with damping.....	2
Note S4.	Motion artifact suppression in respiration analysis based on wavelet coherence.....	4
Note S5.	Detection of Body Orientation	5
Note S6.	Hidden Markov Model with Gaussian Mixture Emissions.....	5
Fig. S1.	Optimized mechanical designs for the electrical interconnects.	7
Fig. S2.	The strain distribution in the Cu layer of the interconnect after stretching to 11 mm.....	8
Fig. S3.	The strain distribution in the Cu layer for the device after deformations.	9
Fig. S4.	Mechanical testing of the devices with hollow and solid silicone elastomer enclosure.....	10
Fig. S5.	FEA results of the devices with different FPCBs thicknesses under different modes of mechanical loading.....	11
Fig. S6.	Experimental comparison between the frequency responses of a hollow packaged device and a mechanically independent accelerometer.....	12
Fig. S7.	Schematic illustration of the vibration model of a one-dimensional rod with damping.....	13
Fig. S8.	The acceleration of the elastomer as a function of the applied frequency for the hollow package and without a device.....	14
Fig. S9.	Histogram of the time lag results from cross correlations between the pulses from the suprasternal notch (SN) and from the chest.....	15
Fig. S10.	Short-time windowed (0.2 s) spectrum of z-axis acceleration measured from the SN of five subjects across different ages and genders.....	16
Fig. S11.	Demonstration of the effect of mounting location.....	17
Fig. S12.	Device sensitivity test to 100 Hz ambient TV sound.....	18
Fig. S13.	Device sensitivity test to vocal sound.	19
Fig. S14.	Bland-Altman analysis for RR under different activities.....	20
Fig. S15.	Bland-Altman analysis for HR and RR during the 7 h sleep study.	21
Fig. S16.	Feature extraction and classification of sleep stages.....	22
Fig. S17.	Cross-sectional schematic illustration of the architecture of the system.	23
Fig. S18.	Demonstration of the effect of strain isolation.	24
Fig. S19.	The stress distributions on the skin with a strain isolation layer.	25
Fig. S20.	The stresses on the skin from the 10% stretched device without a strain isolation layer.	26
Fig. S21.	Experimental comparison between the frequency responses of a normal device and a 12% stretched device.....	27
Fig. S22.	Applying CWT subtraction methods to simulation and experimental signal.	28
Table S1.	The demographic and sample size information of all participants.....	29

Note S1. System Operation Flow

Wireless charging circuit The wireless charging circuit consists of a full-wave rectifier (FWR), low-dropout-regulator (LDO), a Schottky diode, and power-management circuit for charging (PMIC-C) the battery. The FWR converts the input 13.56 MHz alternating current (AC) from the coil to direct current (DC). The LDO regulates the DC input to 5 V (~10 mA) DC output. The DC output flows through the Schottky diode and delivers the charges to PMIC-C. The PMIC-C, then, regulates the power to charges the Li-ion battery according to the voltage level of the battery.

System power management The power from Li-ion battery goes through the DC/DC converter that regulates it to 3.2 V (~2 mA) and delivers to the active components throughout the system, which includes a microcontroller (MCU), accelerometer, and flash memory.

Device operation The user interface controls the device operation. To turn on the system, it first connects to the device. By default, the accelerometer digitally senses 3-axis 1600 Hz accelerometer data and the device streams the 20 Hz downsampled data to the phone along with its battery level without saving the data to the on-board memory. Using the blue "Start Session" and the red "Stop Session" button, the user interface starts and stops recording the data to an on-board flash memory within the device and the recording status toggles accordingly (Fig. 1c). When the session begins, the MCU receives the data from the accelerometer and writes it to the 2 Gb flash memory. During the recording session, pressing the event logging buttons mark the time of specific incidents, arbitrarily assigned to each button. When the session ends, the user interface downloads the data from the device via Bluetooth. The interface can also control multiple devices simultaneously and in time synchronized manner.

Note S2. Finite element analysis

The commercial software ABAQUS (ABAQUS Analysis User's Manual 2010, V6.10) was used to design the device and optimize its mechanical performance. The objectives are to ensure that (1) the Cu layer in the interconnects remains elastic, i.e., no plastic deformation, and (2) minimize the normal and shear stresses on the human skin to achieve a low somatosensory perception when the device undergoes different types of external loads (stretching, bending, and twisting). The epoxy, silicone elastomer (Ecoflex), and silicone gel were modeled by hexahedron elements (C3D8R) while the thin Cu layer and PI films were modeled by composite shell elements (S4R). The number of elements in the model was $\sim 2 \times 10^7$, and the minimal element size was 1/8 of the width of the narrowest interconnects (100 μm). The mesh convergence of the simulation was guaranteed for all cases. The elastic modulus (E) and Poisson's ratio (ν) are $E_{\text{Cu}}=119 \text{ GPa}$, $\nu_{\text{Cu}}=0.34$, $E_{\text{PI}}=2.5 \text{ GPa}$, $\nu_{\text{PI}}=0.34$, $E_{\text{Gel}}=5 \text{ kPa}$, $\nu_{\text{Gel}}=0.49$, $E_{\text{Ecoflex}}=60 \text{ kPa}$, $\nu_{\text{Ecoflex}}=0.49$, $E_{\text{Epoxy}}=22 \text{ GPa}$ and $\nu_{\text{Epoxy}}=0.32$.

Note S3. The theoretical vibration model of a one-dimensional rod with damping

For one-dimensional vibration of a viscoelastic rod, the displacement takes the form $u=f(x)e^{i\omega t}$, where t is time, ω is the angular frequency, and $f(x)$ depends on the x coordinate. The relation between strain ε and displacement u , constitutive model (Kelvin-Voigt model), and dynamic equation of motion are

$$\varepsilon = \frac{\partial u}{\partial x} \quad (1)$$

$$\begin{aligned} \sigma &= E\varepsilon + \eta \frac{\partial \varepsilon}{\partial t} \\ &= (E + i\omega\eta) \frac{\partial u}{\partial x} \end{aligned} \quad (2)$$

$$\frac{\partial \sigma}{\partial x} = \rho \frac{\partial^2 u}{\partial t^2} \quad (3)$$

respectively, where σ is the stress, and E , ρ and η are the Young's modulus, mass density, and viscoelastic damping coefficient, respectively.

Substitution of Eq. (2) into Eq. (3) gives

$$\frac{\partial^2 u}{\partial x^2} = \frac{1}{c^2} \frac{\partial^2 u}{\partial t^2} \quad (4)$$

where

$$c = \sqrt{\frac{E + i\omega\eta}{\rho}} \quad (5)$$

For the problem shown in Fig. S7, the displacement and stress boundary conditions at $x = 0$ and $x = L$ are given by

$$\begin{cases} u(0, t) = u_0 e^{i\Omega t} \\ \sigma(L, t) = -M \frac{\partial^2 u(x, t)}{\partial t^2} \Big|_{x=L} \end{cases} \quad (6)$$

where u_0 and Ω are the magnitude and the angular frequency of the excitation load (from the vibration platform) applied to the rod at $x = 0$. M is the mass per unit area, which represents the mass of the device over the area of its bottom layer

The Fourier transform

$$\begin{aligned} \hat{u}(x, \omega) &= \int_{-\infty}^{+\infty} u(x, t) e^{-i\omega t} dt \\ u(x, t) &= \frac{1}{2\pi} \int_{-\infty}^{+\infty} \hat{u}(x, \omega) e^{i\omega t} d\omega \end{aligned} \quad (7)$$

applied to Eq. (4) gives

$$\frac{d^2 \hat{u}}{dx^2} + k^2 \hat{u} = 0 \quad (8)$$

where $k = \frac{\omega}{c}$. The boundary conditions in Eq. (6) become

$$\begin{cases} \hat{u}(0, \omega) = 2\pi u_0 \delta(\omega - \Omega) \\ \hat{\sigma}(L, \omega) = -M(-i\omega)^2 \hat{u}(L, \omega) = M\omega^2 \hat{u}(L, \omega) \end{cases} \quad (9)$$

where $\delta(x)$ is the Dirac Delta function.

The solution of Eq. (8) is

$$\begin{aligned} \hat{u}(x, \omega) &= C_1 e^{ikx} + C_2 e^{-ikx} \\ \hat{\sigma}(x, \omega) &= ik(E + i\omega\eta)(C_1 e^{ikx} - C_2 e^{-ikx}) \end{aligned} \quad (10)$$

where the coefficients C_1 and C_2 are determined by the boundary conditions (9) to (10) as

$$\begin{cases} C_1 = \frac{[ik(E + i\omega\eta) + M\omega^2] e^{-ikL} \pi u_0 \delta(\omega - \Omega)}{ik(E + i\omega\eta) \cos(Lk) - iM\omega^2 \sin(Lk)} \\ C_2 = \frac{[ik(E + i\omega\eta) - M\omega^2] e^{ikL} \pi u_0 \delta(\omega - \Omega)}{ik(E + i\omega\eta) \cos(Lk) - iM\omega^2 \sin(Lk)} \end{cases} \quad (11)$$

Substituting Eq. (11) into Eq. (10) yields

$$\hat{u}(x, \omega) = \left\{ \begin{aligned} &\frac{[ik(E + i\omega\eta) + M\omega^2] e^{-ikL} e^{ikx}}{ik(E + i\omega\eta) \cos(Lk) - iM\omega^2 \sin(Lk)} \\ &+ \frac{[ik(E + i\omega\eta) - M\omega^2] e^{ikL} e^{-ikx}}{ik(E + i\omega\eta) \cos(Lk) - iM\omega^2 \sin(Lk)} \end{aligned} \right\} \pi u_0 \delta(\omega - \Omega) \quad (12)$$

The Fourier Transform of the acceleration $a(x, t) = \partial^2 u(x, t) / \partial t^2$ is

$$\hat{a}(x, \omega) = (-i\omega)^2 \hat{u}(x, \omega) \quad (13)$$

Its inverse transform gives the acceleration

$$a(x, t) = \frac{1}{2\pi} \int_{-\infty}^{+\infty} \left\{ -\pi u_0 \omega^2 \delta(\omega - \Omega) \left[\frac{[ik(E + i\omega\eta) + M\omega^2] e^{-ikL} e^{ikx}}{ik(E + i\omega\eta) \cos(Lk) - iM\omega^2 \sin(Lk)} + \frac{[ik(E + i\omega\eta) + M\omega^2] e^{ikL} e^{-ikx}}{ik(E + i\omega\eta) \cos(Lk) - iM\omega^2 \sin(Lk)} \right] \right\} e^{i\omega t} d\omega \quad (14)$$

which can be further expressed as

$$a(x, t) = -u_0 \Omega^2 e^{i\Omega t} \left\{ \frac{\sqrt{(E + i\omega\eta) \rho} \cos\left[\frac{(x-L)}{c} \Omega\right] + M\Omega \sin\left[\frac{(x-L)}{c} \Omega\right]}{\sqrt{(E + i\omega\eta) \rho} \cos\left(\frac{L}{c} \Omega\right) - M\Omega \sin\left(\frac{L}{c} \Omega\right)} \right\} \quad (15)$$

The acceleration at the $x=L$ is

$$a(L, t) = \frac{-u_0 \Omega^2 e^{i\Omega t} \left(\frac{L}{c} \Omega\right)}{\left(\frac{L}{c} \Omega\right) \cos\left(\frac{L}{c} \Omega\right) - \left(\frac{LM\Omega^2}{E + i\omega\eta}\right) \sin\left(\frac{L}{c} \Omega\right)} \quad (16)$$

For the displacement at the other end $x=0$ to take the form $u(0, t) = \text{Re}\{u_0 e^{i\Omega t}\} = u_0 \cos(\Omega t)$, the above acceleration at the end $x=L$ is simplified to

$$a(L, t) = \text{Re} \left\{ \frac{-u_0 \Omega^2 e^{i\Omega t} \left(\frac{L}{c} \Omega\right)}{\left(\frac{L}{c} \Omega\right) \cos\left(\frac{L}{c} \Omega\right) - \left(\frac{LM\Omega^2}{E + i\omega\eta}\right) \sin\left(\frac{L}{c} \Omega\right)} \right\} \quad (17)$$

Note S4. Motion artifact suppression in respiration analysis based on wavelet coherence

In the approach reported in the main text, the continuous wavelet transform (CWT) subtraction algorithm aims to exploit time-synchronized three-axis acceleration measurements to extract respiration signal at all activity levels. The detection mechanism relies critically on the suprasternal notch (SN) mounting location and orientation, where the z-axis and x-axis measurements are both sensitive to chest-wall motion, while the y-axis acceleration is mainly associated with core-body motions. The goal is to find the common mode between z-axis and x-axis motion but differential mode between z-axis and y-axis motion.

The wavelet cross spectrum of two time series, x_n and y_n , where $n = 1, 2, \dots, N$ is:

$$C_{xy}(b, n) = C_x^*(b, n) C_y(b, n) \quad (18)$$

where $C_x(b, n)$ and $C_y(b, n)$ denotes the CWT of x and y at scales b and positions n . The superscript denotes the complex conjugate. The coherence projection for the common mode signal embedded in y_n becomes,

$$C_{y'}(b, n) = \frac{C_{xy}^*(b, n)}{C_{xx}(b, n)} \cdot C_x(b, n) \quad (19)$$

We kept wavelet transform coefficients with wavelet coherence $R_{xy}^2(b, n) > 0.8$, where

$$R_{xy}^2(b, n) = \frac{|C_x^*(b, n) C_y(b, n)|^2}{|C_x(b, n)|^2 |C_y(b, n)|^2} \quad (20)$$

For the specific application in suppressing motion artifacts occurring in the frequency range of respiration cycles, the computation uses Morlet wavelets. We chose a sampling period $\Delta t = 20$ s to cover all time scale of interest. The smallest scale for the Morlet wavelets is $s_0 = 2\Delta t$. The CWT discretizes scales with 16 voices per octave. The number of octaves is set to be the nearest integer less than or equal to $\log_2 N - 1$, which in this case is 10. We perform the continuous wavelet transforms as well as a smoothing operation over 16 scales using the built-in MATLAB™ function “cwt” and “smoothCFS”.

In practice, the wavelet transform projection yields common mode z' values between z - and x -axis measurements. The differential mode z'' between z' and y -axis measurements decouple motions from respiration, according to

$$C_{z'} = \frac{C_{xz}}{C_{zz}} \cdot C_z, \quad (21.1)$$

$$C_{z''} = \left(1 - \frac{C_{yz'}}{C_{z'z'}}\right) \cdot C_{z'}. \quad (21.2)$$

Fig. S22a demonstrates an application of the algorithm to simulated signals. Two time-series data, x and z are generated. Both data carry a large amplitude chirp signal in common to mimic the time non-stationary motion artifact, as well as a random gaussian noise of same distribution. A differential sinusoidal signal is added to z to simulate the respiration signal. The algorithm detects the common mode chirp signal between x and z and recovers the differential sinusoidal signal with gaussian noise in z . Fig. S22b presents the subtraction results from sample experimental measurement, using the three-axis acceleration data acquired from a healthy-normal subject during walking. The algorithm suppresses the fast motion artifacts and recovers the slower respiration patterns. Fig. S22c shows a sample detection for zero-crossing nodes using sample extracted respiration signal. A dynamic threshold, set as a tenth of the standard deviation of data collected for 1 min, eliminates the effects of small-amplitude ripples that appear on top of the general respiration pattern.

Note S5. Detection of Body Orientation

We analyze body orientation in $SO(3)$ by finding the rotation matrix transforming the nominal gravity vector in the canonical frame $\mathbf{g} = [0, 0, g_0]$ to the gravity vector measured in the device frame $\mathbf{g}' = [a_x, a_y, a_z]$, where the magnitude of gravity is estimated as $g_0 = \sqrt{a_x^2 + a_y^2 + a_z^2}$. We use Rodrigues' rotation formula for computation efficiency¹,

$$\mathbf{v}_{rot} = \mathbf{v} \cos \theta + (\mathbf{k} \times \mathbf{v}) \sin \theta + \mathbf{k}(\mathbf{k} \cdot \mathbf{v})(1 - \cos \theta) \quad (22)$$

where \mathbf{k} is the unit vector representing the rotation axis around which vector \mathbf{v} rotate an angle θ following right-hand rule. Eq. 22 can be represented in matrix notation, $\mathbf{v}_{rot} = \mathbf{R}\mathbf{v}$, where \mathbf{R} is the rotation matrix,

$$\mathbf{R} = \mathbf{I} + (\sin \theta) \mathbf{K} + (1 - \cos \theta) \mathbf{K}^2 \quad (23)$$

In the above equation, \mathbf{I} is the 3×3 identity matrix, \mathbf{K} is the skew-symmetric cross-product matrix of $\mathbf{k} = [k_1, k_2, k_3]$,

$$\mathbf{K} = \begin{bmatrix} 0 & -k_3 & k_2 \\ k_3 & 0 & -k_1 \\ -k_2 & k_1 & 0 \end{bmatrix} \quad (24)$$

Given the two gravity vectors \mathbf{g} and \mathbf{g}' , we compute rotation axis and angle using cross product and dot product of normalized vectors $\hat{\mathbf{g}}$ and $\hat{\mathbf{g}}'$,

$$\mathbf{k} = \frac{\hat{\mathbf{g}} \times \hat{\mathbf{g}}'}{|\hat{\mathbf{g}} \times \hat{\mathbf{g}}'|}, \sin \theta = |\hat{\mathbf{g}} \times \hat{\mathbf{g}}'|, \cos \theta = \hat{\mathbf{g}} \cdot \hat{\mathbf{g}}'. \quad (25)$$

If we let \mathbf{K}' be the skew symmetric matrix of $\hat{\mathbf{g}} \times \hat{\mathbf{g}}'$, i.e. $\mathbf{K}' = |\hat{\mathbf{g}} \times \hat{\mathbf{g}}'| \mathbf{K}$. Substituting all expressions to Eq. 23, we obtain rotation matrix,

$$\mathbf{R} = \mathbf{I} + \mathbf{K}' + \frac{(1 - \hat{\mathbf{g}} \cdot \hat{\mathbf{g}}') \mathbf{K}'^2}{|\hat{\mathbf{g}} \times \hat{\mathbf{g}}'|^2} \quad (26)$$

We convert the rotation matrix to the corresponding Euler angles in the device frame using MATLAB™ function “rotm2eul”. The rotation angle around the longitudinal axis of body indicates the body orientation of major interest in the sleep study.

Note S6. Hidden Markov Model with Gaussian Mixture Emissions

Sleep scoring involves modeling time series sequences with discrete states. Markov chains are one of the most straightforward statistical approaches to determine the likelihood of a sequence of states. Realistically, MA signal features would not tell sleep stages deterministically. We introduce Hidden Markov Model with Gaussian mixture emissions (GMMHMM) to capture the stochastic emission from states to observations. A Hidden Markov Model (HMM) $\Phi = (\mathbf{A}, \mathbf{B}, \pi)$ encodes a joint probability distribution of generative states sequences $\Omega = \{1, 2, 3, \dots, N\}$ characterized by a set of output observation symbols $\mathbf{O} = \{o_1, o_2, \dots, o_M\}$ with an underlying probabilistic dependence. We let s_t denote the state at time t . In the mathematical representation, $\mathbf{A} = \{p_{ij}\}$ is a transition probability matrix, where p_{ij} is the transition probability from state i to j . $\mathbf{B} = \{q_{ik}\}$ is the output probability distribution, where q_{ik} is the probability of

emitting observation symbol o_k in state i . $\pi = P(s_0 = i)$ is the initial state distribution. Sleep stage identification is a learning problem, *i.e.* given a sequence of observations $\mathbf{X} = (X_1, X_2, \dots, X_T)$, to find the best characteristic model parameter Φ' so that the joint probability $\prod P(X|\Phi)$ is optimized through expectation-maximization (EM) algorithm. For the specific application, we use `sklearn.hmm.GMMHMM` module to train the HMM parameters and infer the hidden states. We randomly initialize the HMM parameter values. The prior distribution over initial states is uniform. The EM algorithm runs for 10 iterations or until convergence.

In the sleep study, the input features to the GMMHMM model take the form of multi-frequency band signal power, characterized by the band-limited root mean square (BLRMS) in 120-s time epoch, as our input features to the GMMHMM model. The band choices feature the 0.1-0.8 Hz respiration signals, as well as the 20-50 Hz cardiac signals. We choose in total seven bands for a balance between the characterization of system complexity and the feature representation for generality. Fig. S16a shows the full feature extraction filter-bank. Fig. S16b shows the time-series of each band power for the sample 7-hour sleep data presented in the main text, Fig. 5.

For the HMM model, we set the number of states to be $N = 5$. Multi-band z-axis signal power on a logarithmic scale serves as the observable clustering features to classify the five sleep stages labeled as 0 to 4 from Wake to Rapid Eye Movement (REM). The multi-band choices are 0.1-0.8 Hz for respiration, sub-bands in the range 0.8-20 Hz for body motions, and 20-80 Hz for cardiac activity. Gaussian mixture emissions determine the probability of multi-band power observations given the state. The inferred hidden states capture the overall trend of clinician determined sleep scoring.

The HMM model developed upon small dataset is a simple clustering method providing no information about the labeling. We permute the inferred states for all combinations of labeling and assign each class to a stage according to a minimum marathon distance optimization. Fig. S16c presents the final classification result in comparison with the clinically determined sleep stages. Fig. S16c summarizes the success rate in a confusion matrix.

Supplementary Reference

1. Murray, R. M., Li, Z. & Shankar Sastry, S. *A Mathematical Introduction to Robotic Manipulation* (CRC press, 2017). <https://doi.org/10.1201/9781315136370>

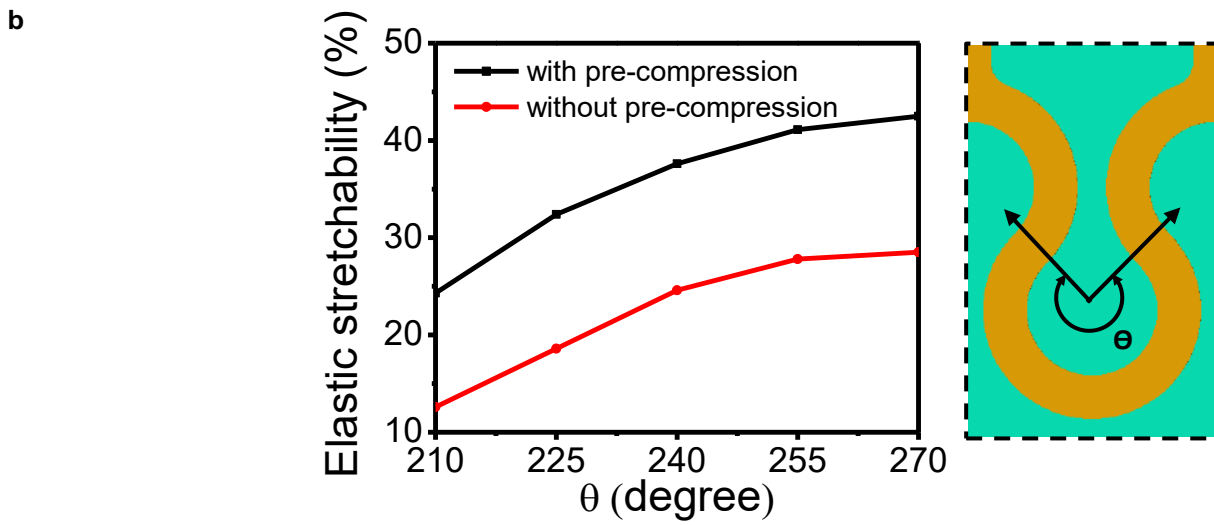
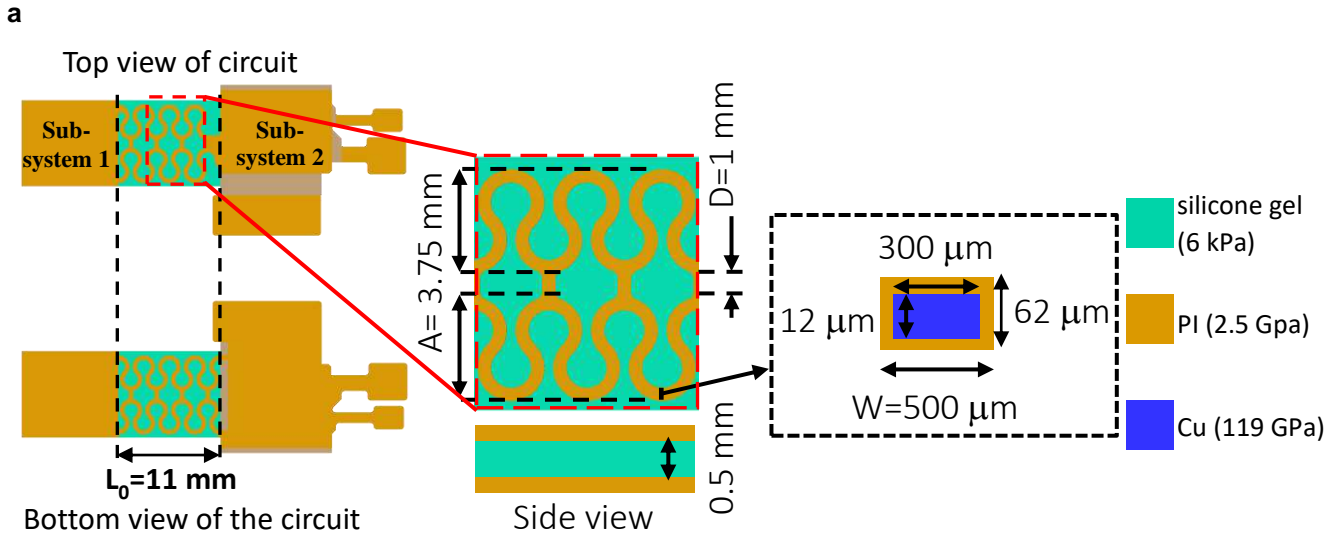


Fig. S1. Optimized mechanical designs for the electrical interconnects. (a) Schematic illustration of a double layer serpentine interconnect with an arc angle of 270° **(b)** Relationship between the arc angle and the elastic stretchability of the interconnects with and without pre-compression.

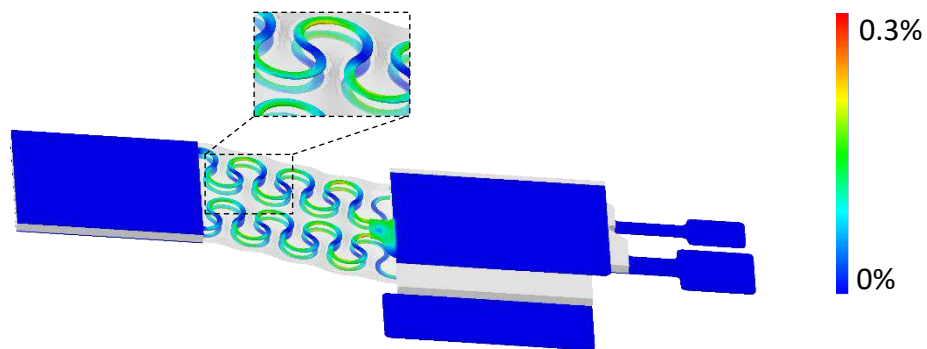


Fig. S2. The strain distribution in the Cu layer of the interconnect after stretching to 11 mm. The interconnects straighten back to their nominal (non-buckled) length from the pre-buckled state at 11% strain of the overall device.

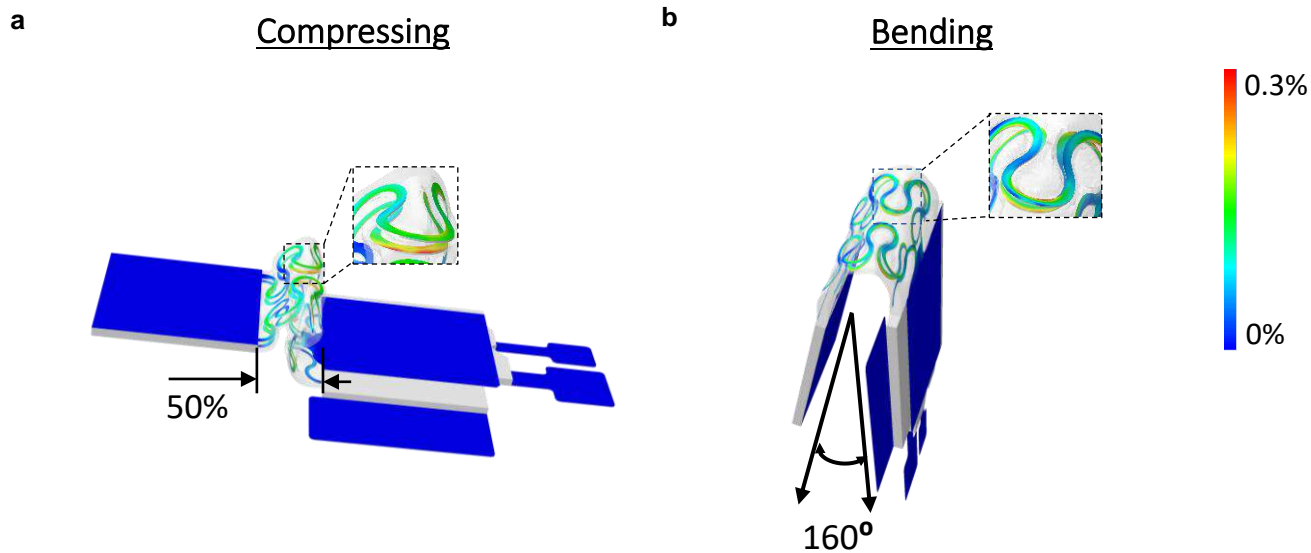


Fig. S3. The strain distribution in the Cu layer for the device after deformations. **(a)** 50% compression and **(b)** 160° bending angle. For both loading cases, the computed strain in the Cu layer of interconnects is lower than the 0.3% yielding strain

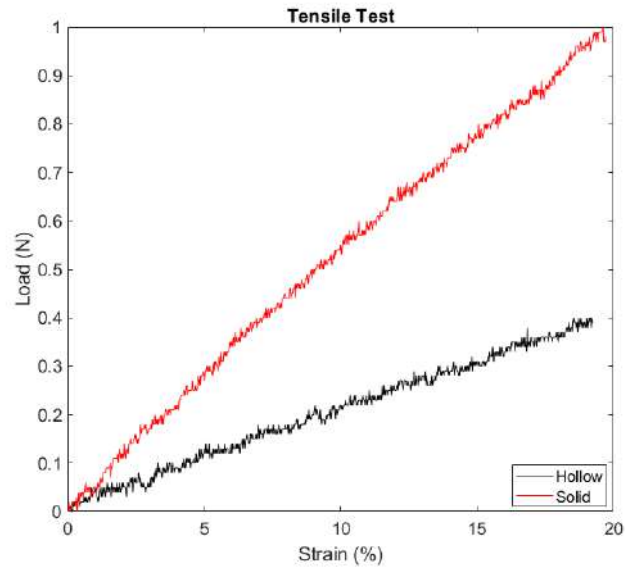


Fig. S4. Mechanical testing of the devices with hollow and solid silicone elastomer enclosure. The solid silicone elastomer enclosure is much stiffer than the hollow enclosure under tension.

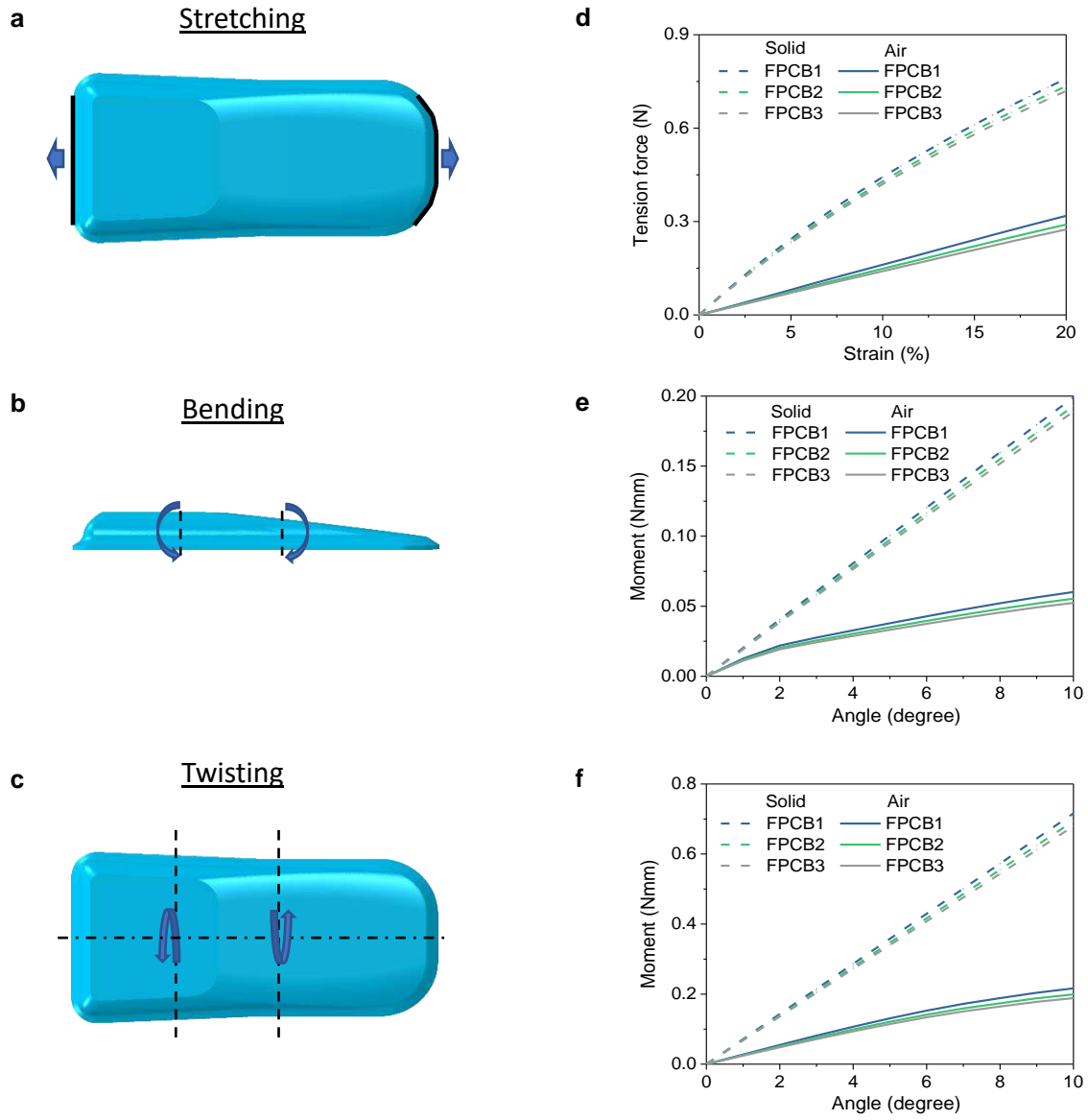


Fig. S5.FEA results of the devices with different FPCBs thicknesses under different modes of mechanical loading. Illustration of device under different modes of load: **(a)** stretching, **(b)** bending, and **(c)** twisting on the devices with different FPCBs thicknesses (FPCB1: 12 μm PI/ 25 μm Cu/ 12 μm PI; FPCB2: 8.69 μm PI/ 20 μm Cu/ 8.69 μm PI; FPCB3: 5.79 μm PI/ 12.5 μm Cu/ 5.79 μm PI). **(d)** Tensile force as a function of the applied strain for the solid and hollow package with a 61 kPa and 18 kPa equivalent tensile modulus for the devices with FPCB1 respectively. **(e)** Moment as a function of the bending angle for the solid and hollow package configurations with a 11 Nmm^2 and 6.8 Nmm^2 equivalent bending stiffness for the devices with FPCB1 respectively. **(f)** Moment as a function of the twisting angle for the solid and hollow package configurations with a 38 Nmm^2 and 15 Nmm^2 equivalent twisting stiffness for the devices with FPCB1 respectively. The results for stretching, bending, and twisting deformation show that the thickness of the layers has a small influence (less than 10% difference) in the equivalent tensile modulus, bending, and twisting stiffness for these three FPCBs.

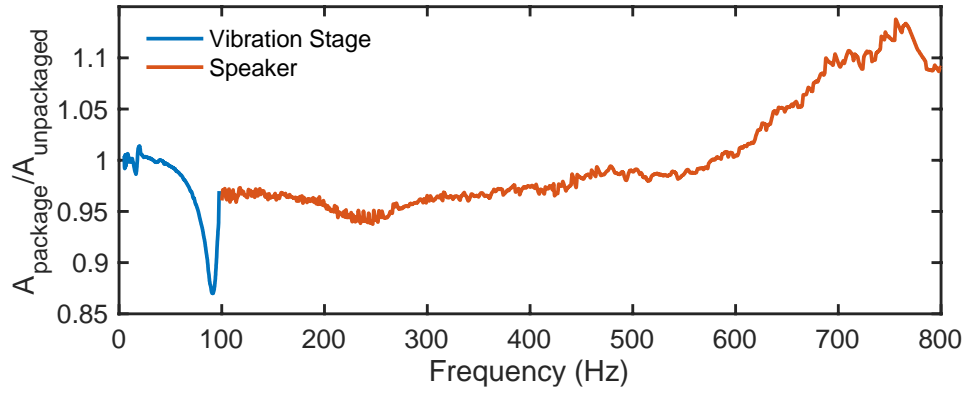


Fig. S6. Experimental comparison between the frequency responses of a hollow packaged device and a mechanically independent accelerometer. The ratio between the frequency response of a hollow packaged device A_{package} and that of an unpackaged accelerometer $A_{\text{unpackage}}$ stays close to 1 in the frequency range of interest (0-800 Hz), except for a maximum of ~13% drop in the relative response around 91 Hz due likely to a resonance; the encapsulated device is more sensitive than the unpackaged one at high frequencies (>600 Hz). The driving sources for the frequency sweep tests are a vibration stage (3B, Scientific) (1-100 Hz) and a speaker (100-800 Hz).

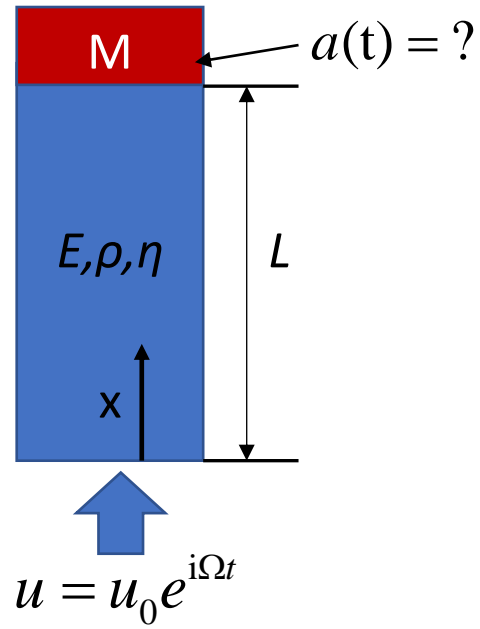


Fig. S7. Schematic illustration of the vibration model of a one-dimensional rod with damping. The parameters of the model are described next. E , ρ and η are the Young's modulus, mass density and damping coefficient, respectively. L and M are the length of the substrate and mass of the device per unit area. The amplitude and angular frequency of the applied excitation is given by u_0 and Ω respectively. x and t are the spatial coordinates and time

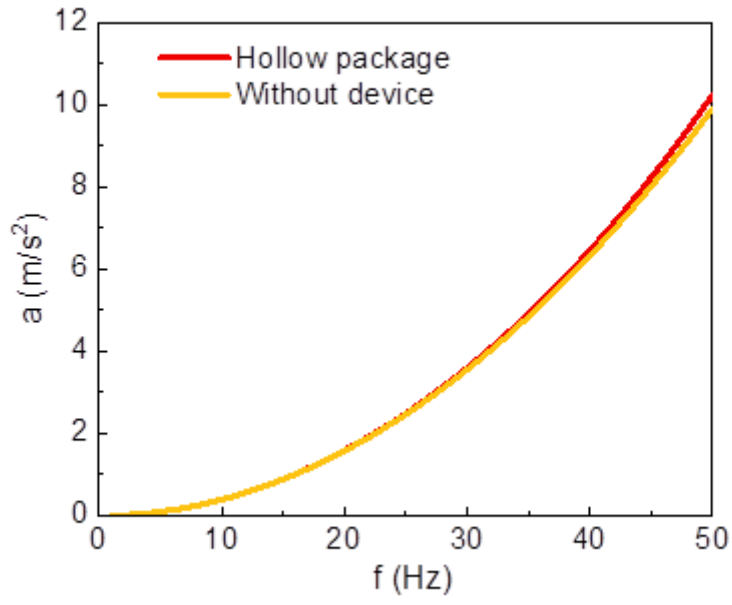


Fig. S8. The acceleration of the elastomer as a function of the applied frequency for the hollow package and without a device. The parameters used in the simulation are $E = 60 \text{ kPa}$, $\rho = 1070 \text{ kg/m}^3$, $L = 2 \text{ mm}$, $M_{\text{hollow}} = 0.01 \text{ g/mm}^2$ which represents the weight of the device over the area of its bottom layer, $u_0 = 0.1 \text{ mm}$, and the damping ratio ($\xi = \eta\omega$) was 0.03.

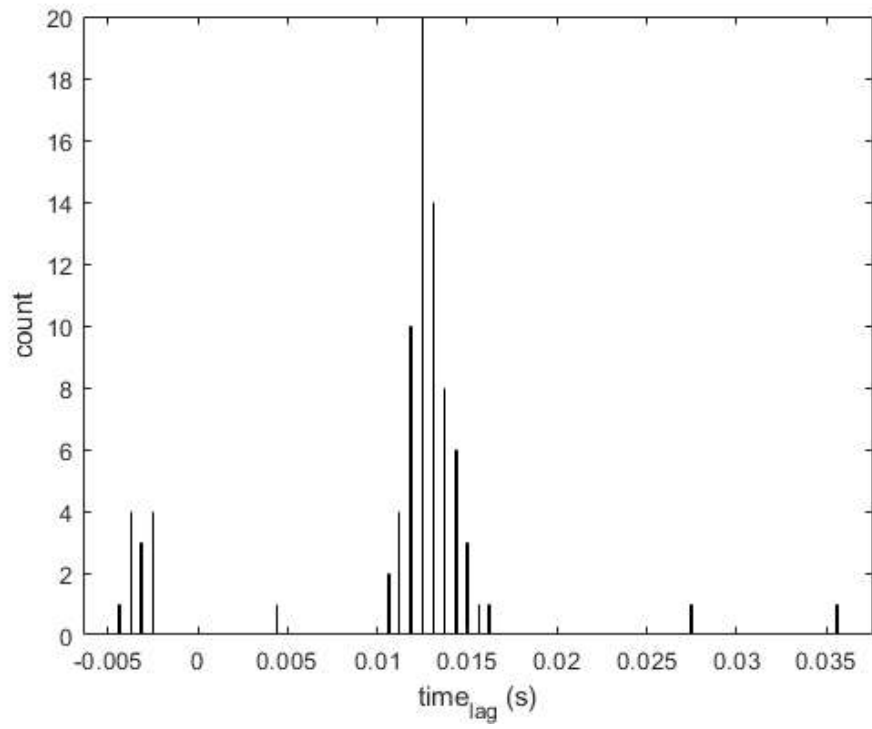


Fig. S9. Histogram of the time lag results from cross correlations between the pulses from the suprasternal notch (SN) and from the chest. The SN has the time lag of ~13 ms. This indicates that the vibratory signatures related to the pulsatile flow of blood are from the carotid artery as opposed to chest/body vibrations due directly to the heartbeat.

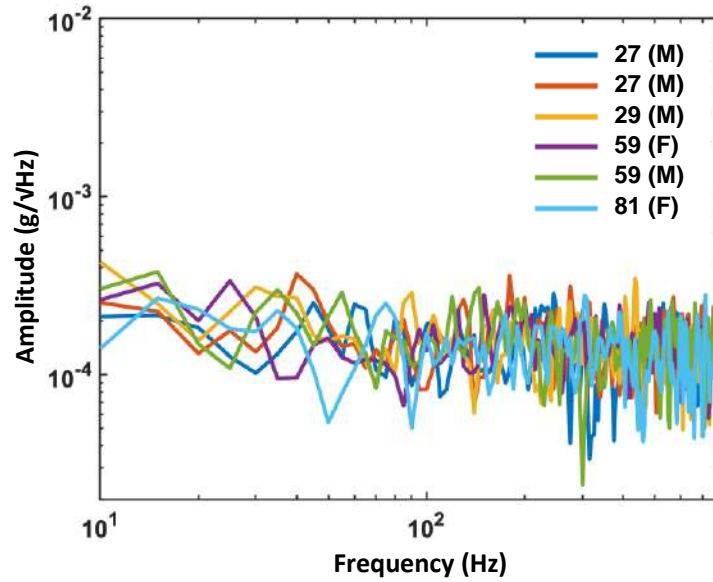
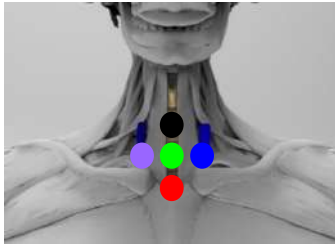


Fig. S10. Short-time windowed (0.2 s) spectrum of z-axis acceleration measured from the SN of five subjects across different ages and genders. Data from male (M) and female (F) subjects from 27 to 81 years old, each while sitting quietly in a resting state. The analysis windows are manually chosen from time periods where no bio-signals are clearly present. The spectrums indicate a noise behavior of the device close to that on the Ecoflex (Fig. 2a), which exhibit no clear difference between different age groups.



— Middle — High
 — Low — Right
 — Left

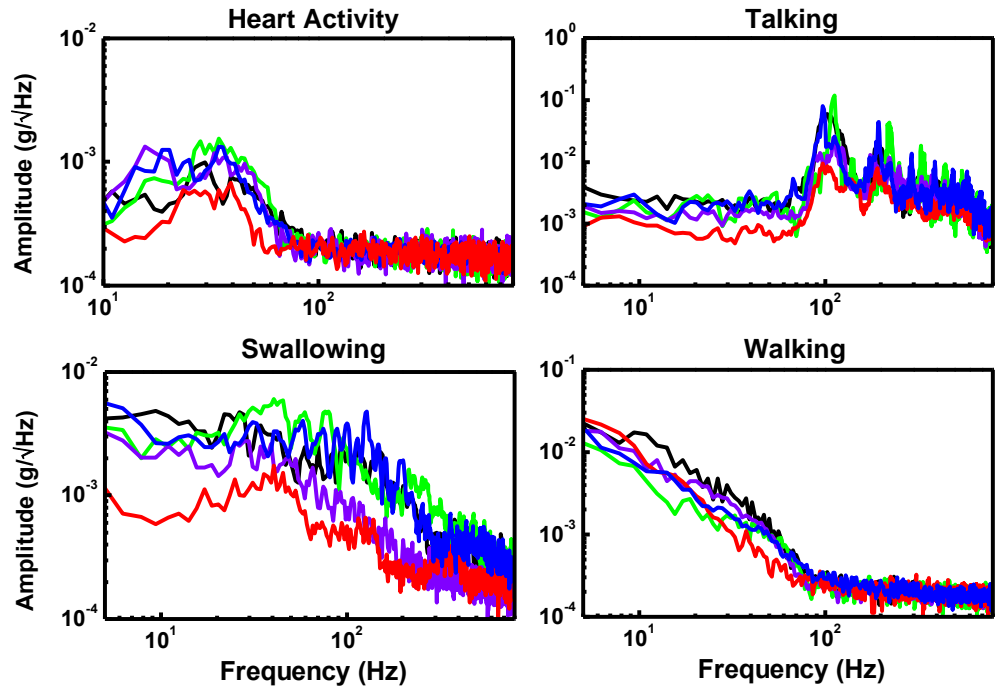
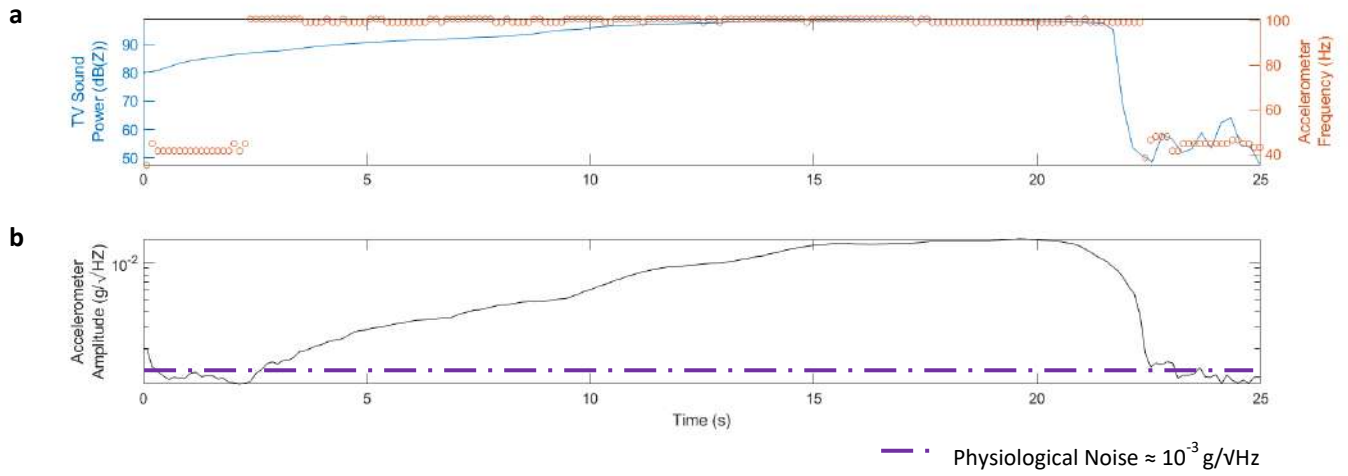


Fig. S11. Demonstration of the effect of mounting location. The measurements are from five different locations (± 1 cm vertical and horizontal displacements from the center of the SN) of a male subject with lower body mass. The results indicate that the device is not sensitive to the mounting locations, especially for the prominent frequency range for each distinctive event. There are slight differences in the magnitude of the signal relative to the position which agrees with the anatomical locations of the associated signal sources.



*Physiological Noise \approx HR maximum amplitude in 20 – 50 Hz

Fig. S12. Device sensitivity test to 100 Hz ambient TV sound. (a) The device is responsive to ambient sound that is louder than 87 dBZ, which was measured by the microphone. **(b)** Even though the device picks up the ambient sound starting at 87 dBZ, its effect in the accelerometer amplitude is not significant until it reaches 98 dBZ. Even when the ambient sound reaches the power of 98 dBZ, the accelerometer amplitude (2×10^{-2} g/√Hz) is smaller than that of the general speech signal (10^{-1} g/√Hz).

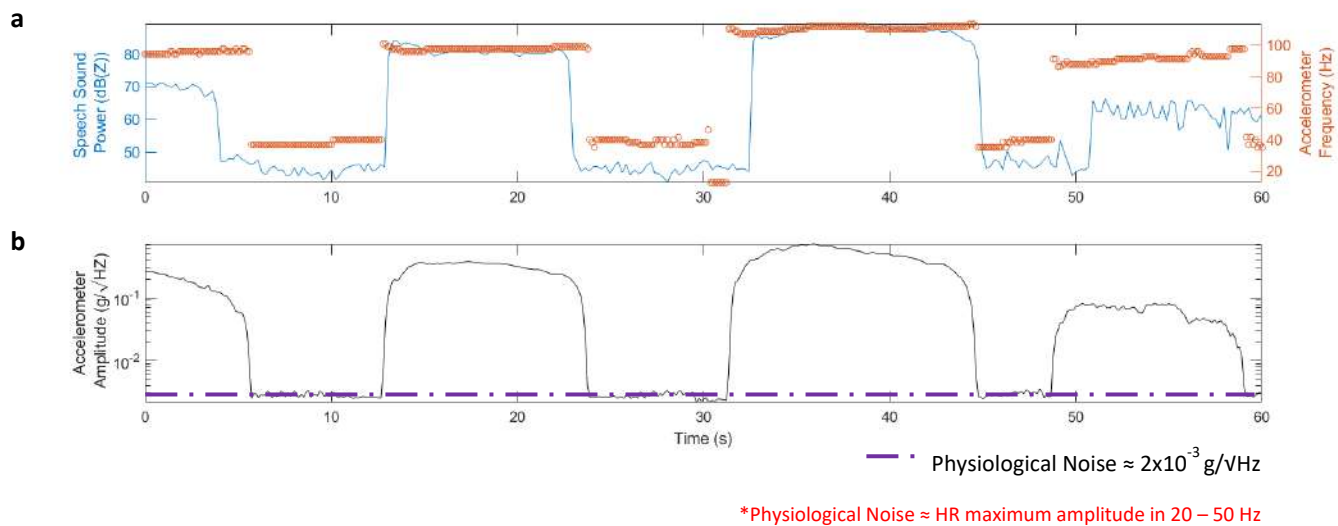


Fig. S13. Device sensitivity test to vocal sound. (a) The device is sensitive to vocal sound that is softer than 65 dBZ, which was measured by the microphone. **(b)** Even when the vocal sound is ~65 dBZ, the device picks up the vocal fold vibration with the adequate amplitude ($10^{-1} \text{ g}/\sqrt{\text{Hz}}$) for the signal processing algorithm.

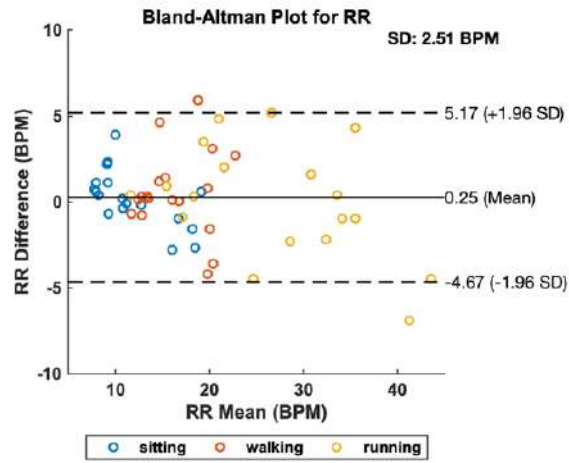


Fig. S14. Bland-Altman analysis for RR under different activities. For sitting, the mean difference between MA and reference measurements is 0.21 BPM and the standard deviation $A_{\text{RMS}} = 1.63$ BPM (N=18); for walking, the mean difference is 0.52 BPM, and $A_{\text{RMS}} = 2.43$ BPM (N=19); for running, the mean difference is 0.01 BPM and $A_{\text{RMS}} = 3.34$ BPM (N=19). N indicates the sample size for each scenario.

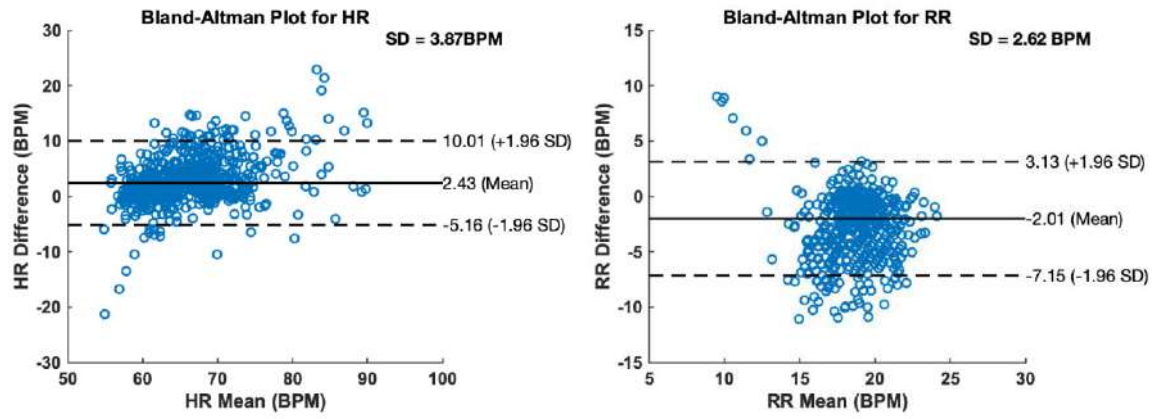


Fig. S15. Bland-Altman analysis for HR and RR during the 7 h sleep study. HR has a mean difference of 2.4 BPM and a standard deviation A_{RMS} of 3.9 BPM ($N = 853$). RR has a mean difference of -2.0 BPM and a standard deviation of 2.6 BPM ($N = 853$). N indicates the sample size for each scenario.

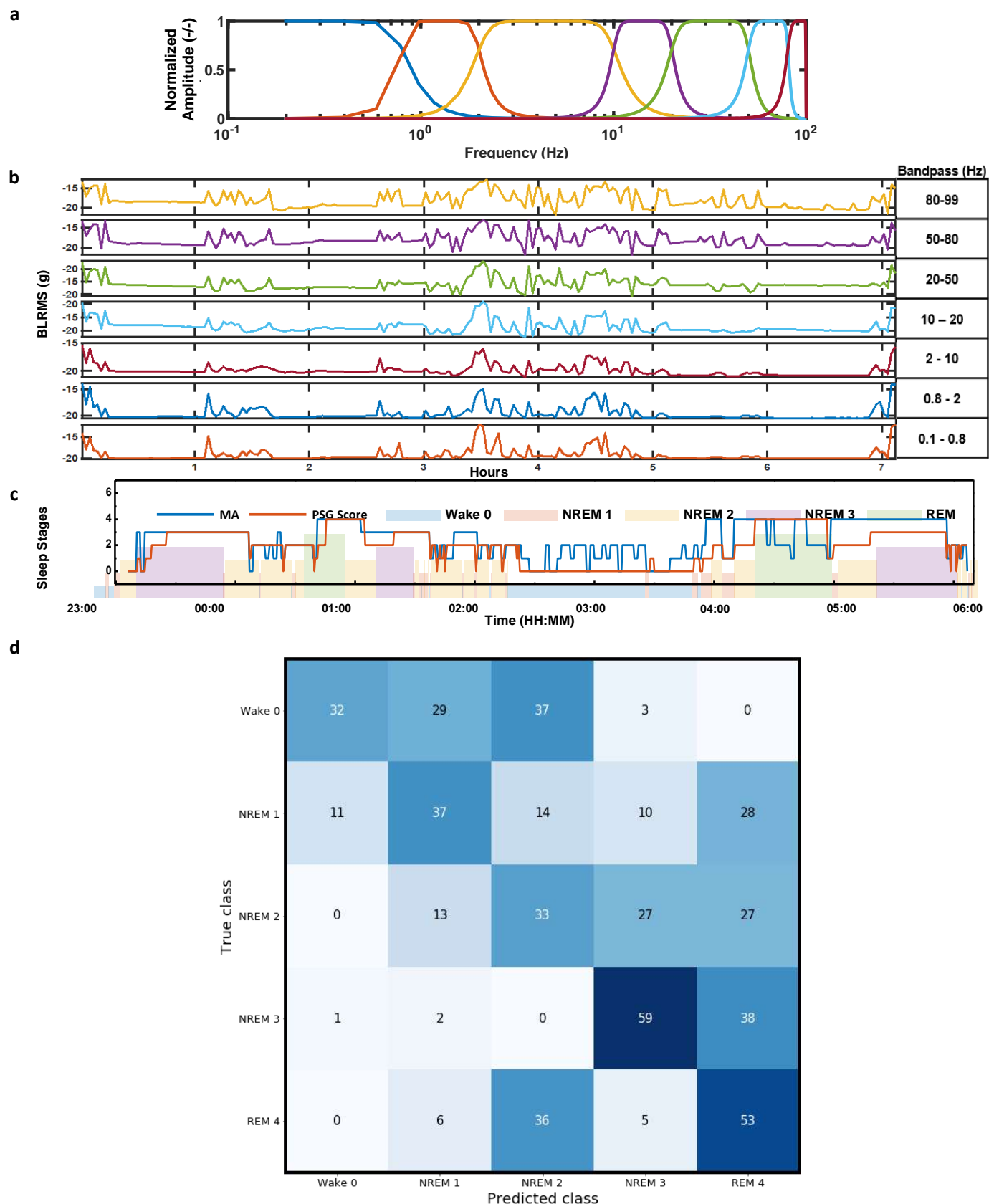


Fig. S16. Feature extraction and classification of sleep stages. (a) The filter-bank for energy feature generation (b) The time series of multi-band energy extracted from z-axis acceleration measurements. (c) The inference of sleep stages based on the multi-band signal power in comparison with clinically determined sleep stages. (d) The confusion matrix for the success rate of the classification.

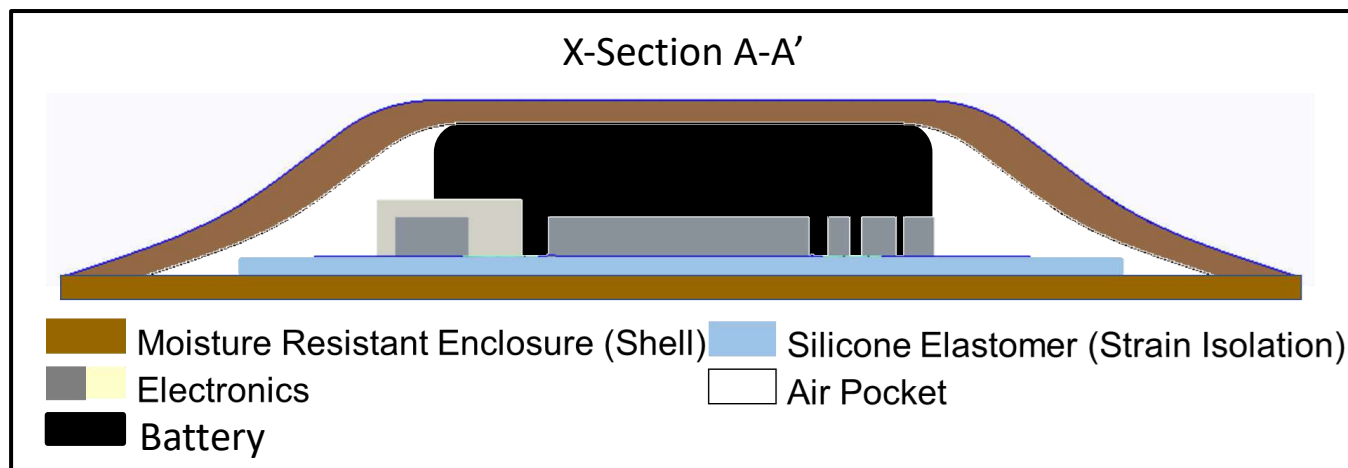


Fig. S17. Cross-sectional schematic illustration of the architecture of the system. A thin membrane (300 μm) of a low modulus formulation of silicone (Ecoflex) forms an air pocket, or hollow enclosure. The hollow enclosure construction minimizes mechanical constraints of the serpentine interconnects during the device deformations.

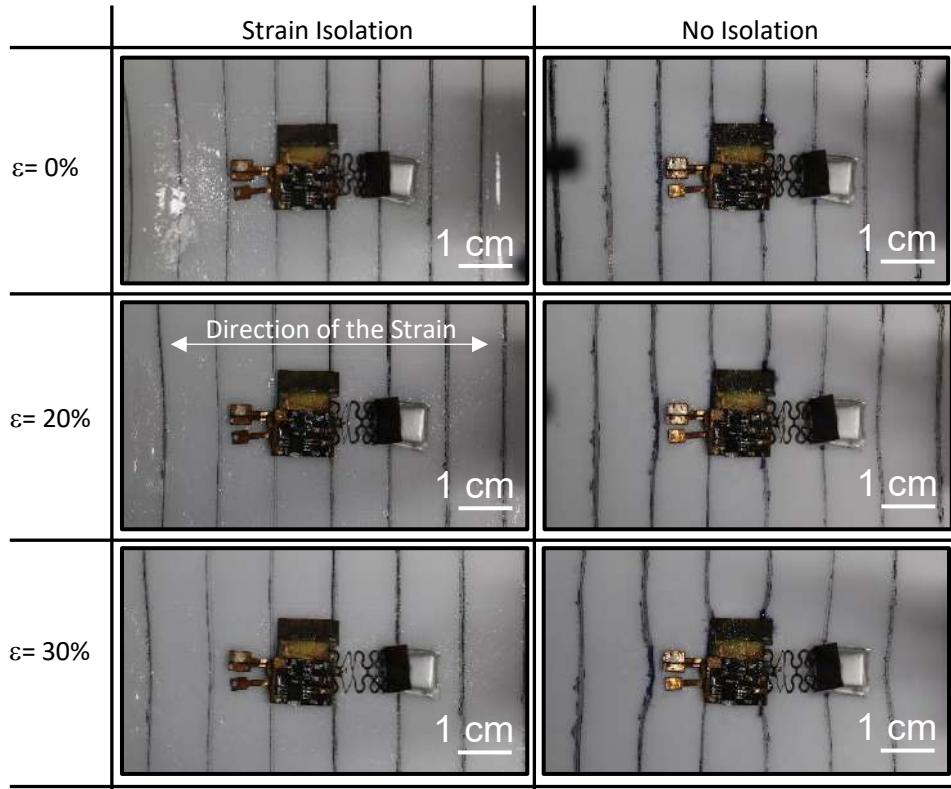


Fig. S18. Demonstration of the effect of strain isolation. Devices with and without strain isolation are mounted to an underlying silicone elastomer with vertical line markings to illustrate the effect of the strain isolation layer. Strain isolation minimizes deformations in the silicone elastomer that otherwise results from the rigid islands that support the electronic components.

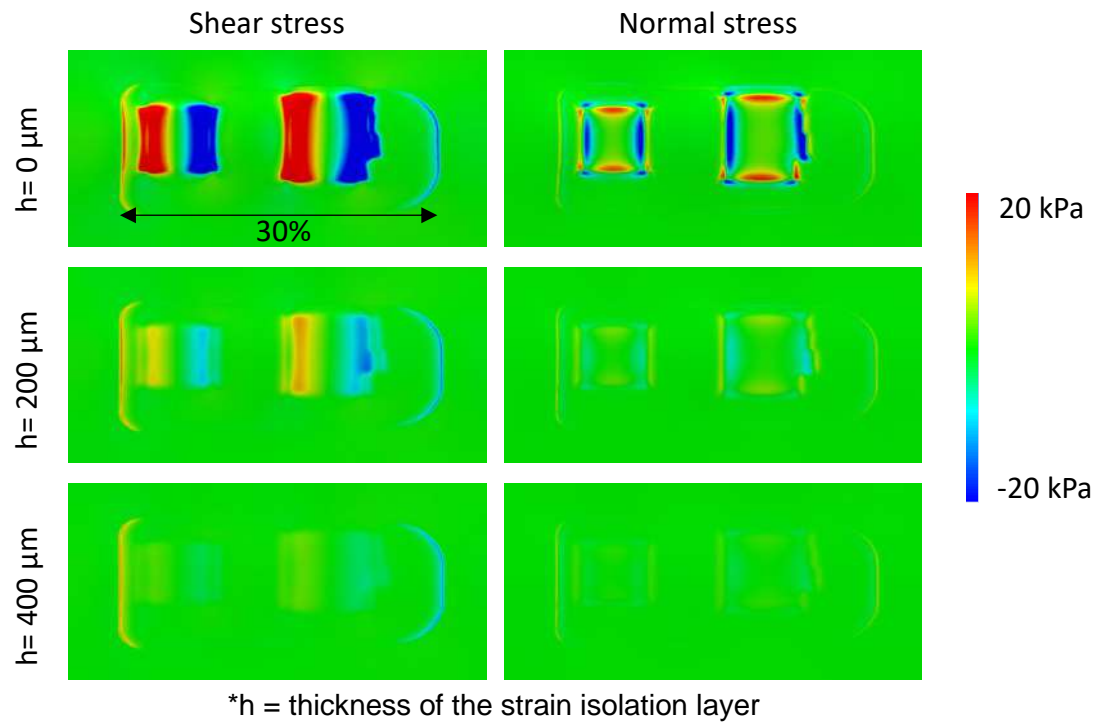


Fig. S19. The stress distributions on the skin with a strain isolation layer. The color indicates stress on the skin induced by stretching the device by 30% when different strain isolation layer thicknesses ($h = 0, 200$, and $400 \mu\text{m}$) are used.

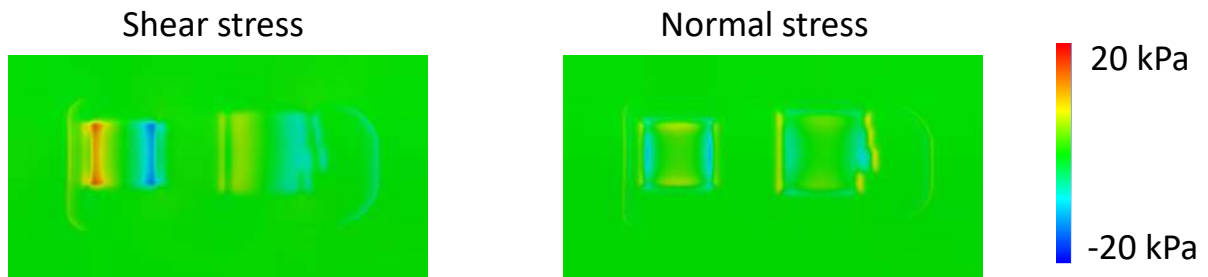


Fig. S20. The stresses on the skin from the 10% stretched device without a strain isolation layer. The device without the strain isolation layer induces stress on the skin even at low tensile strain.

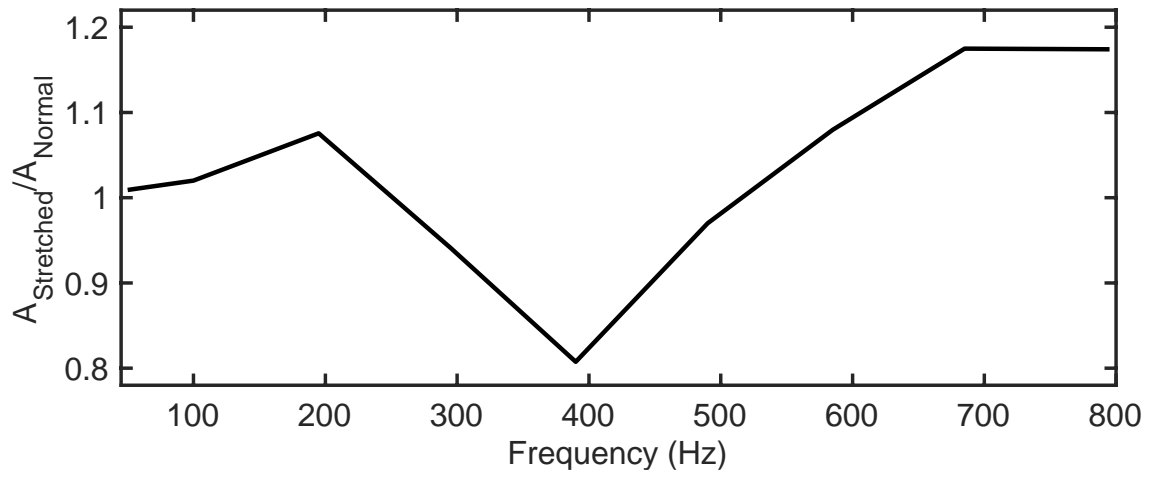


Fig. S21. Experimental comparison between the frequency responses of a normal device and a 12% stretched device. The ratio between the frequency response of a 12% stretched device $A_{\text{Stretched}}$ and that of a normal device A_{Normal} stays close to 1 across the frequency range (0-800 Hz) except for a maximum of ~20% drop around 400 Hz. The stretched device becomes more sensitive at high frequencies (>500 Hz). The stretched device also delaminates at a higher frequency (>295 Hz) and causes transient instability.

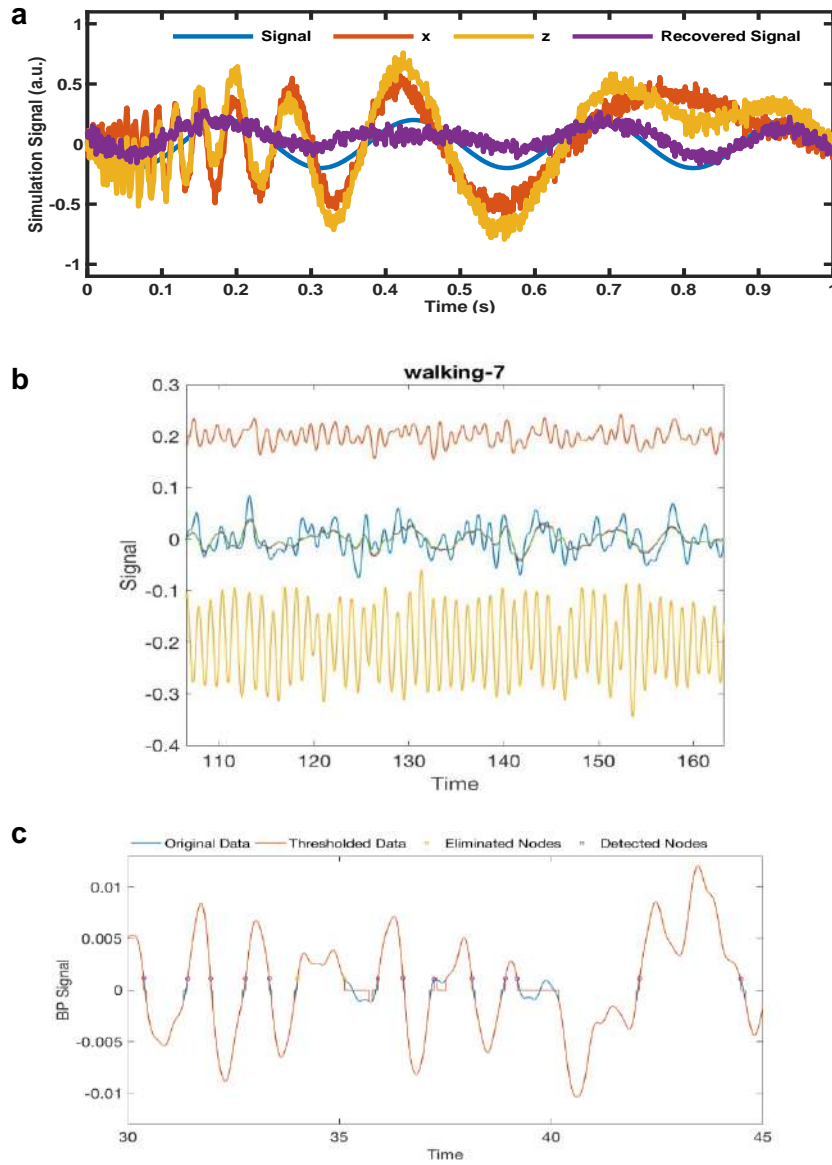


Fig. S22. Applying CWT subtraction methods to simulation and experimental signal. (a) A numerical simulation test for performance of wavelet cross spectrum analysis. The algorithm detects the common mode (a large amplitude chirp) between X and Z and recovers the differential sinusoidal signal embedded in Z. **(b)** A sample wavelet cross spectrum analysis for chest-wall motion decoupling using three-axis acceleration measurements. The 0.1-1 Hz band-passed x- and y-axis data is offset by 0.2 g for visualization purposes. **(c)** Zero-crossing nodes detected from the extracted signal. A dynamic threshold equal to a tenth of the standard deviation of 1 min data eliminates the effects of small-amplitude ripples that appear on top of the general respiration pattern.

Table S1. The demographic and sample size information of all participants.

Cycling	Respiration	Dining
Subject 1 (N=60)	Subject 1 (N=18)	Subject 1 (N=5)
Subject 2 (N=60)	Subject 2 (N=10)	Subject 2 (N=6)
Subject 3 (N=60)	Subject 3 (N=7)	Subject 3 (N=4)
Subject 4 (N=60)	Subject 6 (N=12)	Subject 4 (N=6)
Subject 5 (N=61)	Subject 7 (N=5)	Subject 8 (N=5)

Subject	Age	Gender	Race	Ethnicity
Subject 1 (David)	21	Male	Asian	Filipino-Chinese
Subject 2 (Xiaoyue)	28	Female	Asian	Chinese
Subject 3 (Mohan)	26	Female	Asian	Chinese
Subject 4 (Peter)	26	Male	Asian	Korean
Subject 5 (Jiahong)	22	Male	Asian	Chinese
Subject 6 (Marc)	21	Male	Black	Afro-Puerto Rican
Subject 7 (Esther)	21	Female	Asian	Korean
Subject 8 (Jeremy)	20	Male	White	Argentine American